Ore Geology Reviews 99 (2018) 180–194

Contents lists available at ScienceDirect

Ore Geology Reviews

journal homepage: www.elsevier.com/locate/oregeorev

Origin of the Muguayuan veinlet-disseminated tungsten deposit, South China: Constraints from in-situ trace element analyses of scheelite

Xiao-Yu Li[a], Jian-Feng Gao[b,*], Rong-Qing Zhang[a], Jian-Jun Lu[a,*], Wen-Hui Chen[c], Jin-Wei Wu[a]

[a] State Key Laboratory for Mineral Deposits Research, School of Earth Sciences and Engineering, Nanjing University, Nanjing 210023, China
[b] State Key Laboratory of Ore Deposit Geochemistry, Institute of Geochemistry, Chinese Academy of Sciences, Guiyang 550081, China
[c] No. 418 Geological Team of Bureau of Geology and Mineral Exploration and Development of Hunan Province, China

ARTICLE INFO

Keywords:
In-situ LA-ICP-MS analyses
Trace elements
Fluid evolution
Muguayuan scheelite deposit
South China

ABSTRACT

The Late Triassic Muguayuan W deposit is located in the middle of the Jiangnan Orogen, South China. This deposit is characterized by veinlet-disseminated W mineralization that developed in the Sanxianba granitic porphyry stock. The ore minerals are mainly scheelite with minor molybdenite and wolframite. Scheelite mineralization was closely related to greisenization and phyllic alteration, and took place in two stages. Stage I involved scheelite ± wolframite ± molybdenite + quartz veinlet and disseminated mineralization, whereas Stage II resulted in scheelite + quartz + sericite veinlet mineralization. Sulfide and quartz + calcite ± pyrite veinlets formed during the post-ore stage. Scheelites from the two mineralization stages have different textures and compositions. Cathodoluminescence (CL) images of Stage I scheelites reveal two generations of growth (I-a and I-b). Stage I-a scheelite is dark under CL with oscillatory zoning, and has light rare earth element (LREE)-enriched chondrite-normalized patterns, negative Eu anomalies, and high total REE contents. Stage I-b scheelite forms rim overgrowths on Stage I-a scheelite, is bright under CL, and shows positive Eu anomalies and relatively low REE contents. Although Stage II scheelites are nearly uniform under CL, they can be subdivided into two generations according to their REE systematics. Stage II-a scheelite yields middle REE (MREE)-enriched chondrite-normalized patterns, with negative Eu anomalies, whereas Stage II-b scheelite has MREE-depleted patterns with positive Eu anomalies. Minor amounts of apatite formed in both stages of mineralization. Stage I apatite contains 1370–1930 ppm Mn and 97.7–127 ppm Sr, whereas Stage II apatite has lower Mn (111–158 ppm) and higher Sr (2170–4690 ppm) concentrations. The distinct trace elements compositions of the scheelite and apatite from the two stages identify two ore-forming fluids that had different origins and compositions. The ore-forming fluids in Stage I-a were relatively reduced magma-derived fluids with high Mo, Mn, Nb, and Ta, and low Sr. Fluid modeling shows that the initial fluids of Stage I-a were LREE-enriched with negative Eu anomalies, similar to the Sanxianba granitic porphyry. Precipitation of early apatite and scheelite, as well as plagioclase decomposition, altered the fluid composition and led to relative depletions in REE, Nb, and Ta, and increases of Eu and Sr in the Stage I-b fluids. Cooling of these fluids and the addition of recycled meteoric water led the fluids to become relatively oxidized and Sr-rich; Stage II scheelite precipitated from these fluids. Precipitation of Stage II-a scheelite resulted in the Stage II-b fluids becoming progressively MREE-depleted. Extensive alteration, especially greisenization and phyllic alteration, led to plagioclase decomposition, which provided the Ca necessary for scheelite mineralization. This process was important in generating the W mineralization in the Muguayuan deposit, and perhaps for other granite-hosted, veinlet-disseminated scheelite deposits in the Jiangnan Orogen.

1. Introduction

Scheelite deposits occur mainly as skarn and veinlet-disseminated types. Scheelite skarns are hosted in carbonate-rich rocks at or near the contacts with granitic intrusions, and the Ca-rich wall rocks are thought to be essential for scheelite precipitation (Gaspar and Inverno, 2000; Mao and Li, 1996; Werner et al., 2014; Wu et al., 2014). Veinlet-disseminated scheelite deposits occur mainly in granitic rocks and have previously been considered to be sub-economic (Seedorff et al., 2005; Sinclair et al., 2011). However, in the past decade, some large veinlet-disseminated scheelite deposits have been discovered in the Jiangnan Orogen, South China (e.g., Dahutang, Yangchuling, and Dongyuan; Fu et al., 2011; Huang and Jiang, 2014; Mao et al., 2013, 2017; Xiang et al., 2013), revealing this to be one of the most important W

* Corresponding authors.
E-mail addresses: gaojianfeng@mail.gyig.ac.cn (J.-F. Gao), lujj@nju.edu.cn (J.-J. Lu).

https://doi.org/10.1016/j.oregeorev.2018.06.005
Received 30 December 2017; Received in revised form 22 May 2018; Accepted 2 June 2018
Available online 15 June 2018

mineralization types in the world. For example, the Dahutang deposit has total W (WO_3) resources of > 2 Mt (Mao et al., 2013). These W ore deposit discoveries have led to new research into this type of scheelite mineralization. Unlike scheelite skarn mineralization, veinlet-disseminated scheelite mineralization is developed in granite and granite-granodiorite porphyries. This challenges the previous assumption that Ca-rich sedimentary wall rocks are essential for the formation of large scheelite deposits. A number of petrological, geochemical, and geochronological studies have been carried out on these veinlet-disseminated scheelite deposits (Huang and Jiang, 2014; Mao et al., 2013, 2015; Mao et al., 2017; Wang et al., 2017). However, the origin and evolution of ore-forming fluids in these mineralizing systems remain unclear due to a lack of detailed investigations.

In-situ laser ablation-inductively coupled plasma-mass spectrometry (LA-ICP-MS) trace element analysis of minerals has been widely used to constrain magmatic and hydrothermal processes (Brugger et al., 2000; Ghaderi et al., 1999; Hazarika et al., 2016; Peng et al., 2004; Song et al., 2014; Sun and Chen, 2017; Xiong et al., 2017). Scheelite is a common mineral that forms in various types of hydrothermal deposits, and it can incorporate abundant trace elements, such as rare earth elements (REEs), Sr, Y, Pb, Mn, and Mo, via substitution for Ca^{2+} or W^{6+} in the crystal lattice. These substitutions are controlled mainly by the crystal structure of scheelite and the physicochemical nature of the associated fluids (Brugger et al., 2000, 2008; Ghaderi et al., 1999; Liu et al., 2007; Raimbault et al., 1993; Song et al., 2014; Zhao et al., 2018).

Ghaderi et al. (1999) analyzed the REE compositions of scheelites from orogenic Au deposits and concluded that crystal structure exerts a first-order control on the elemental chemistry of scheelite. Brugger et al. (2000) combined cathodoluminescence (CL) imaging and LA-ICP-MS trace element analyses of scheelite from the Mt. Charlotte and Drysdale Au deposits, Western Australia, and proposed that scheelite chemistry is sensitive to the dynamics of the hydrothermal system. Song et al. (2014) reported that high-Mo scheelite from the skarn-type W-Mo deposits precipitated under oxidizing conditions. Sun and Chen (2017) used scheelite chemistry to show that ore-forming fluids for the giant Dahutang deposit were multistage and derived from multiple sources. Hence, in-situ LA-ICP-MS trace element analyses of scheelite can provide important insights into the origin and evolution of ore-forming fluids in veinlet-disseminated W ore deposits.

The newly discovered Muguayuan W deposit is located in central Hunan Province and is a typical veinlet-disseminated scheelite deposit within the Jiangnan Orogen. In this paper, we describe the geology and ore petrography of the Muguayuan deposit, and present CL imaging and in-situ LA-ICP-MS trace element analyses of scheelite. These observations and data advance our understanding of the evolution of hydrothermal fluids and mineralization processes in this deposit.

2. Geological background

The South China Block (SCB) comprises the Yangtze Block to the northwest and the Cathaysia Block to the southeast (Wang et al., 2007a,b, 2014). At 860–820 Ma, these two blocks collided and amalgamated to form the SCB (Wang et al., 2014; Zhou and Zhu, 1993) along the Jiangnan Orogen (Fig. 1a), which comprises mainly Neoproterozoic lower-greenschist-facies metamorphosed sedimentary rocks along with interbedded mafic-intermediate volcanic and pyroclastic rocks. These rocks have been intruded by undeformed Neoproterozoic granitoids (Wang et al., 2004, 2014; Zhou et al., 2002).

The Central Hunan Metallogenic Province, located in the middle of the Jiangnan Orogen, was intruded by Triassic and subordinate Devonian granitic rocks (Fig. 1b; Chu et al., 2012). There are three types of W mineralization in this province. Sb–Au–W deposits developed in Proterozoic to Paleozoic rocks (Hu et al., 2017), in which scheelite is a minor component. The genetic link between the Sb–Au–W deposits and magmatism is unclear (Ma et al., 2002; Peng et al., 2003). The other two types of W deposits are veinlet-disseminated and skarn types, in which scheelites are the dominant W minerals. These deposits are spatially and genetically related to granitic rocks (Fig. 1b; Xie et al., 2018).

The Muguayuan deposit is a typical veinlet-disseminated W deposit and is located in the northern part of the Central Hunan Metallogenic Province (Fig. 1b). Late Triassic granitoids in this district include the Taojiang granodiorite pluton, the Yanbaqiao granodiorite pluton, and the Sanxianba granitic porphyry stock and dikes (Fig. 1b). The Taojiang pluton, with an exposed area of 239 km^2, is the largest granitic pluton in the district, and was emplaced at ~217 Ma (Wang et al., 2012). The Yanbaqiao pluton has an exposed area of > 70 km^2 and has similar petrological features and emplacement age as the Taojiang pluton (HBGMR, 1988). The Sanxianba granitic porphyry stock is exposed over a small area and is associated with W mineralization in the Muguayuan deposit.

3. Ore deposit geology

The main strata in the Muguayuan W deposit are the Neoproterozoic Lengjiaxi Group, the Madiyi Formation of the Banxi Group, and Quaternary sediments (Fig. 2a). The Lengjiaxi Group comprises silty slate and sericite slate with a thickness of 649 m. The Madiyi Formation consists of gray to green silty slate, with sandstone and arkosic rocks near the base of the formation. The main structure is the Huaqiaogang syncline in the southern part of the deposit (Fig. 2a). The main faults are the WNW-ESE-trending Fault I and NE-SW-trending Fault II. Fault I dips steeply to the northeast and controlls the emplacement of the Sanxianba granitic porphyry stock.

Tungsten mineralization developed in the Sanxianba granitic porphyry stock. The stock has an elongate surface exposure along Fault I, with a length of ~200 m and width of ~45 m (Fig. 2a). The stock has a porphyritic texture (20–60 vol% phenocrysts) and massive structure. Phenocrysts with grain sizes of 0.2–3.0 mm comprise quartz (30–40 vol %), K-feldspar (30–40 vol%), plagioclase (20–30 vol%; An = 30–40), and minor biotite (< 5 vol%) (Fig. 3a–c). The matrix is composed of microcrystalline feldspar, quartz, and mica (Fig. 3a). Accessory minerals include zircon, apatite, ilmenite, and monazite (Fig. 3c). In the east of the ore district, there are several NW-SE-trending granitic porphyry dikes (Fig. 2a) that have similar mineral assemblages to the Sanxianba stock, but do not host W mineralization (No. 418 Geological Team, unpublished report).

The Sanxianba stock is strongly altered, including albitization, greisenization, phyllic alteration, and silicification, amongst which greisenization and phyllic alteration are the most common. Albite occurs as overgrowth rims on plagioclase, or within K-feldspar forming a perthitic texture (Fig. 3b). Greisenization is characterized by the pervasive and micro-veinlet replacement of primary minerals by muscovite and quartz. The pervasive replacement resulted in the formation of sparsely distributed to abundant muscovite produced by the alteration of biotite (Fig. 3d) and feldspar (Fig. 3e). Micro-veinlet replacement is characterized by the development of quartz and muscovite micro-veinlets that cut the granitic rocks (Fig. 3f). Greisenization is always overprinted by phyllic alteration, in which sericite may replace muscovite (Fig. 3g). Phyllic alteration resulted in the formation of sericite-quartz micro-veinlets (Fig. 3h). In some cases, nearly all the primary rock-forming silicates have been replaced by sericite, with quartz being the only primary mineral remaining (Fig. 3i).

Three major ore shoots have been delineated based on W grades (Fig. 2b–c). The total W reserve (WO_3) is 23,300 metric tons (No. 418 Geological Team, unpublished report). The ore minerals are mainly scheelite and minor wolframite, molybdenite, pyrite, and arsenopyrite. Gangue minerals include quartz, muscovite, sericite, and minor ankerite and apatite. Scheelite is present in disseminated form in the altered granitic porphyry, or as aggregates in veinlets (Fig. 4).

Based on crosscutting relationships and mineral assemblages, the following stages of mineralization and veining are recognized.

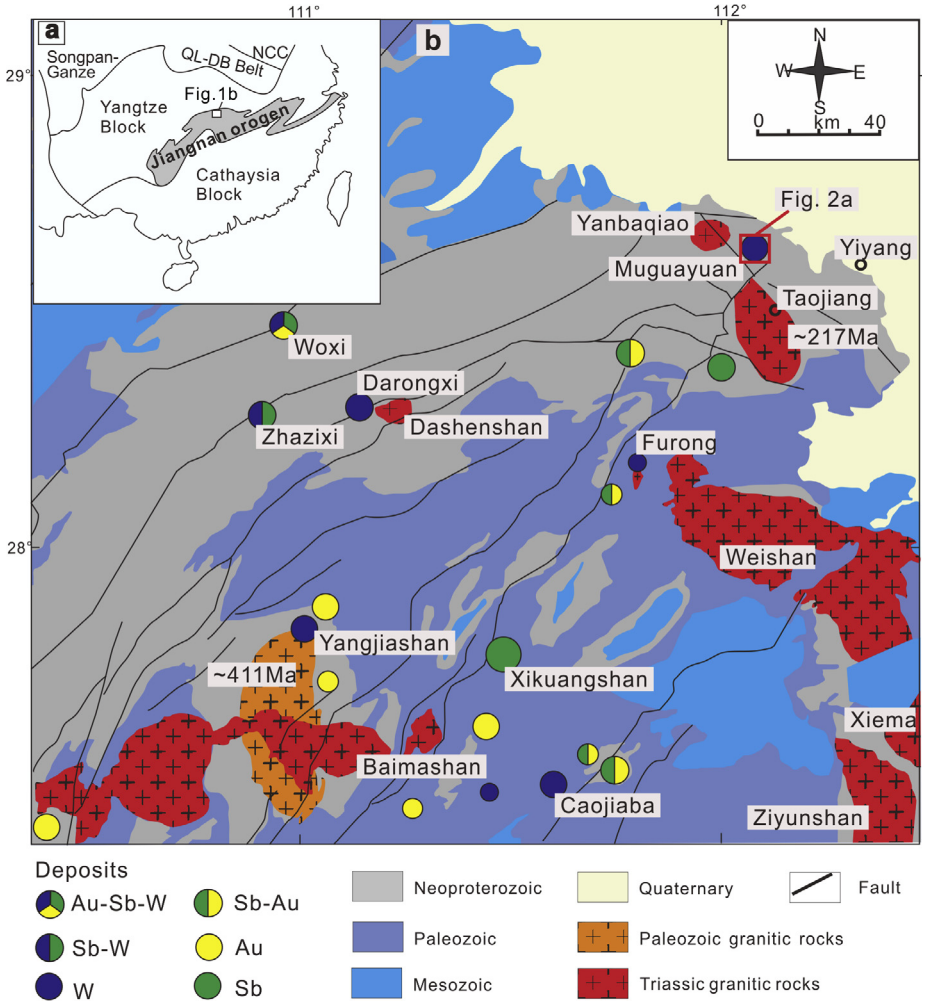

Fig. 1. Regional geological map of the Central Hunan metallogenic province, southern China, showing the distribution of granitic intrusions and important Sb, Au, and W deposits (modified after Xie et al., 2018). Zircon U-Pb age of Taojiang pluton is from Wang et al. (2012). Zircon U-Pb age of Baimashan pluton is from Xie et al. (2018).

(1) Stage I scheelite mineralization: Scheelite mineralization that formed during Stage I is disseminated or present as veinlets, and was associated with greisenization (Figs. 3d–f and 5d). Early scheelite ± wolframite ± molybdenite + quartz veinlets (Stage I) have irregular walls and are 1–5 cm wide (Fig. 4). These veinlets contain scheelite ± wolframite ± molybdenite ± pyrite ± arsenopyrite ± rutile and quartz + muscovite ± apatite ± ankerite (Fig. 5a–d). Scheelite in Stage I veinlets is present as disseminated grains and aggregates (Fig. 4). Wolframite is a residual phase after replacement by scheelite (Figs. 4a and 5a). Molybdenite is present as tiny aggregates (0.1–0.3 cm) on the sidewalls of the veinlets (Fig. 4b). Sporadic pyrite and arsenopyrite are disseminated in the veinlets (Fig. 5b). Rutile is rare and is associated with scheelite (Fig. 5b). The quartz is milky in color (Fig. 4), anhedral, and has a variable grain size (Fig. 5a–d). Muscovite is present as aggregates in the veinlets (Fig. 5d). Stage I apatite is dumpy and occurs interstitially between scheelite grains (Fig. 5c). Anhedral ankerite is associated with the scheelite in the veinlets (Fig. 5a). Scheelite grains are also disseminated in the greisenized granitic porphyry (Fig. 5e) and have similar CL brightness as scheelites in the Stage I veinlets (Fig. 6a–b).

(2) Stage II scheelite mineralization: Scheelite mineralization of Stage II formed mainly veinlets and was closely associated with phyllic alteration (Figs. 3i, 4b, and 5f). Stage II veinlets with widths of 0.1–0.5 cm crosscut Stage I veinlets and have clear contacts with the granitic porphyry (Fig. 4b–c). Scheelite-bearing veinlets of Stage II comprise mainly scheelite, quartz, and sericite, with minor ankerite, pyrite, and apatite. Scheelite is the main ore mineral and is present as continuous veinlets or disseminated grains (Figs. 4b–c, 5f, and 5i). Quartz in the veinlets occurs as anhedral and fine-grained crystals, whereas sericite is typically present in clusters of lobate flakes (Fig. 5f). Apatites in the Stage II veinlets have two different occurrences: intergrown with scheelite (Fig. 5g–h) and interstitial to quartz and scheelite (Fig. 5i). Ankerite crystals are typically interstitial to other minerals (Fig. 5i). Pyrite is fine-grained and found disseminated within the sericite clusters.

(3) Post-mineralization veinlets: In the Muguayuan W deposit, sulfide (pyrite ± galena ± sphalerite) and quartz + calcite ± pyrite veinlets developed during the post-mineralization stage. Both types of post-ore veinlets crosscut the early scheelite-bearing veinlets. Sulfide veinlets are crosscut by late quartz + calcite ± pyrite veinlets (Fig. 4d). Quartz + calcite ± pyrite veinlets develop vugs that are filled by drusy quartz crystals (Fig. 4d).

4. Samples and analytical methods

4.1. Samples

Scheelite samples were selected from the different mineralization stages. Scheelite samples ZK006-34 and ZK0402-41 (Stage I) represent disseminated mineralization. Scheelite samples ZK006-39 and ZK006-

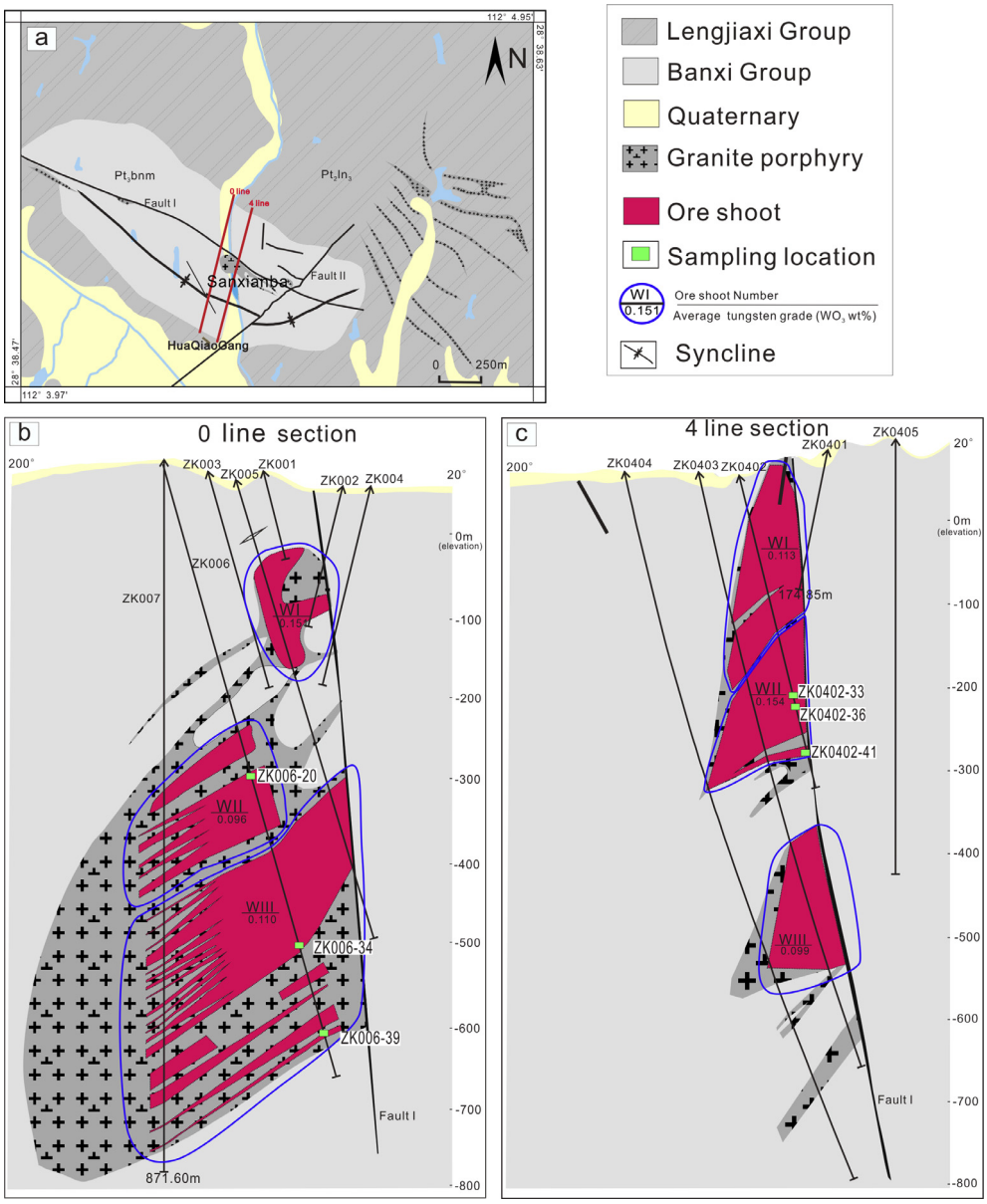

Fig. 2. Geological sketch map of the Muguayuan W deposit (a) and the cross-sections of lines 0 and 4 (b and c) (modified after No. 418 Geological Team, unpublished report).

20 are from Stage I veinlets, and samples ZK0402-33 and ZK0402-36 are from Stage II veinlets. Thin-sections of the selected samples were prepared and polished for CL imaging and in-situ LA-ICP-MS trace element analysis. Apatite grains hosted in magmatic biotite and Stage I and II veinlets were also selected for in-situ LA-ICP-MS analysis.

4.2. Cathodoluminescence imaging

Cathodoluminescence (CL) imaging was employed to reveal the internal textures of minerals for use during micro-analysis (Marshall, 1988). CL images of scheelites were taken with a Carl Zeiss Supra 55 field-emission scanning electron microscope (FE-SEM) coupled to a GATAN MonoCL4 detector at the State Key Laboratory for Mineral Deposits Research in Nanjing University, China. The analysis conditions were an accelerating voltage of 3 kV, working distance of 11.5 mm, and aperture size of 30 μm.

4.3. LA-ICP-MS trace element analysis

Trace element contents of scheelites and apatites were measured with a Photon Machines Excite 193 nm laser ablation system coupled to an Agilent 7700x ICP-MS at the FocuMS Laboratory, Nanjing, China. Helium was used as the carrier gas and argon was the make-up gas. The make-up gas was mixed with the carrier gas via a T-connector prior to entering the ICP source. The instrument settings were optimized whilst ablating the NIST SRM 610 standard, to obtain maximum signal intensities, but keeping oxide (ThO/Th $<$ 0.3%) and doubly charged ion (Ba^{2+}/Ba^{+} $<$ 0.4%) production low. Each analysis incorporated 20 s of background acquisition (gas blank) followed by 40 s of data acquisition whilst ablating the sample. A laser beam with a diameter of 25–40 μm was used to ablate the scheelite grains. Analyses of NIST SRM 610 were performed after every eight sample analyses to correct the data for time-dependent sensitivity drift and mass discrimination (Liu et al., 2008). Raw data reduction was performed off-line by ICPMS-DataCal 10.1 software using the 100%-normalization strategy, without applying internal standard (Liu et al., 2008).

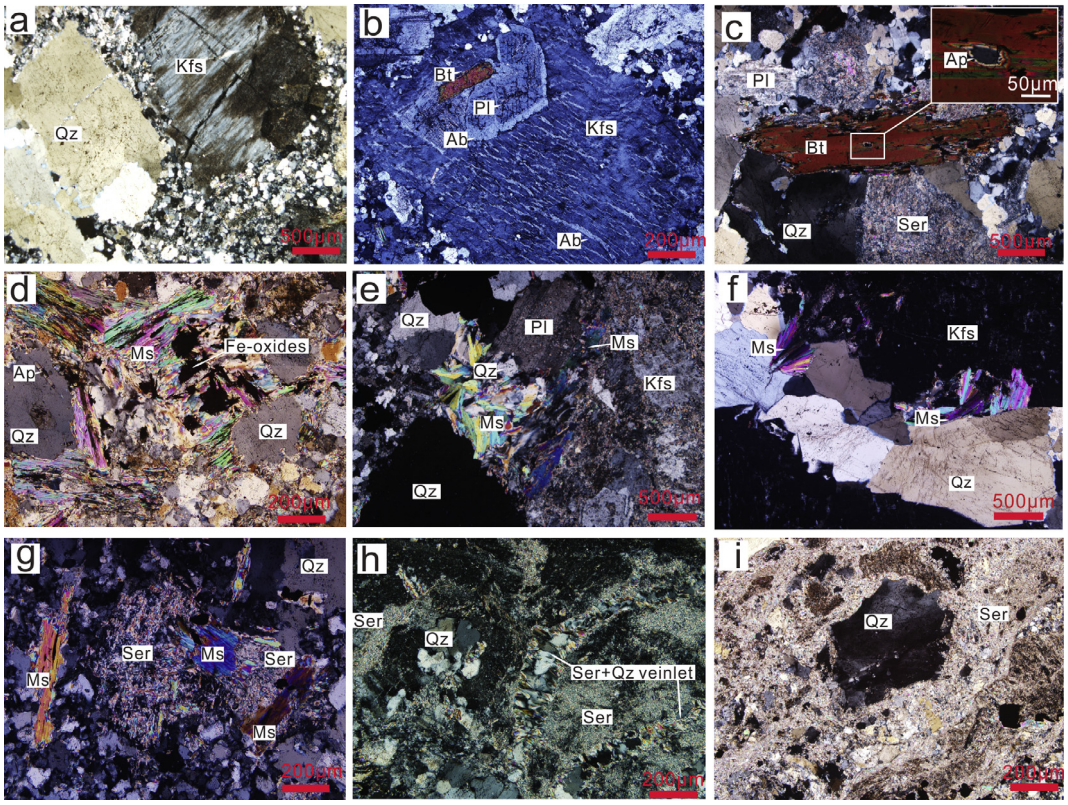

Fig. 3. Photomicrographs of granite porphyry and alteration in the Muguayuan W deposit (crossed polars). (a) Porphyritic texture with quartz and K-feldspar phenocrysts. (b) K-feldspar includes the earlier plagioclase and biotite; albite replaced the plagioclase as overgrowth and K-feldspar as stripes. (c) Biotite phenocryst includes apatite as inclusion. (d) Muscovite replaces biotite, and after biotite alteration, anhedral or sagenitic Fe-oxides (opaque minerals) precipitate. (e) Feldspar is replaced by clusters of muscovite. (f) Quartz + muscovite micro-veinlet crosscuts K-feldspar. (g) Phyllic alteration overprints greisenization. (h) Intense phyllic alteration of the granite porphyry. (i) Intensive phyllic alteration with residual quartz phenocryst. Abbreviations: Ab: albite, Ap: apatite, Bt: biotite, Kfs: K-feldspar, Ms: muscovite, Pl: plagioclase, Qz: quartz, Rt: rutile, Sch: scheelite, Ser: sericite.

5. Results

5.1. Cathodoluminescence imaging of scheelite

Stage I scheelites from disseminated ore (Fig. 6a) and Stage I veinlets (Fig. 6b) have similar CL characteristics. They exhibit two distinct CL domains: inner dark cores (Stage I-a) and outer bright domains (Stage I-b). Scheelites from Stage II veinlets show no obvious CL zoning (Fig. 6c–d). Cathodoluminescence imaging also revealed that some Stage II scheelites may form rim overgrowths or micro-veinlets penetrating the Stage I scheelite in veinlets (Fig. 6b).

5.2. Scheelite and apatite trace element data

Representative trace element analyses of scheelite and apatite are given in Tables 1 and 2, respectively. Chondrite-normalized REE patterns for the scheelite and apatite are presented in Figs. 7 and 8, respectively.

Scheelites from Stages I and II have different REE patterns and trace element compositions. Stage I scheelites are characterized by high ΣREE concentrations (220–4020 ppm; average = 1350 ppm) and light REE (LREE)-enriched patterns (Table 1; Fig. 7a–d). These scheelites have high Mo (3.63–3420 ppm; average = 1080 ppm), Mn (48.1–244 ppm; average = 91.6 ppm), Nb (21.8–266 ppm; average = 120 ppm), and Ta (0.36–11.0 ppm; average = 4.39 ppm), and relatively low Sr (37.7–487 ppm; average = 89.7 ppm) contents (Table 1; Fig. 9). Stage II scheelites have highly variable REE patterns with relatively low ΣREE (23.2–1420 ppm; average = 360 ppm), and have low contents of Mo (average = 3.16 ppm), Mn (0.47–77.3 ppm; average = 8.36 ppm), Nb (2.59–154 ppm; average = 12.2 ppm), and Ta (average = 0.22 ppm), and elevated Sr (60.3–3080 ppm; average = 1910 ppm) contents (Table 1; Figs. 7e–f and 9). From Stage I to II, scheelite Nb and Ta concentrations show a decreasing trend (Fig. 9b).

Stage I scheelites can be divided into Stages I-a and I-b. Stage I-a scheelite has high ΣREE (285–4020 ppm; average = 1490 ppm) and negative Eu anomalies (Eu_N/Eu_N^* = 0.12–0.96; average = 0.38 ppm), whereas Stage I-b scheelite has relatively low ΣREE (230–1020 ppm; average = 610 ppm) and positive Eu anomalies (Eu_N/Eu_N^* = 1.18–8.20; average = 2.82). Stage I-a scheelite has higher concentrations of Nb and Ta, and lower Eu and Sr, than Stage I-b scheelite (Fig. 9b and d).

Large Stage II scheelite grains (Fig. 6e–f) exhibit two types of REE patterns: cores enriched in middle REE (MREE) (Stage II-a) or rims depleted in MREE (Stage II-b) (Fig. 7f). Small isolated scheelite grains (Fig. 6c–d) have MREE-enriched patterns (Fig. 7e) and are considered to be Stage II-a scheelite. Stage II-a scheelite has higher ΣREE (140–1420 ppm; average = 640 ppm) than Stage II-b scheelite (23.2–340 ppm; average = 104 ppm). From Stages II-a to II-b, the MREE (Sm–Ho) contents in the scheelites gradually decrease, and $(La/Sm)_N$ ratios increase (Fig. 9c). Eu anomalies in Stage II-a scheelite are negative (Eu_N/Eu_N^* = 0.27–0.79; average = 0.61), but are mostly positive (Eu_N/Eu_N^* = 0.87–9.12; average = 2.22) in Stage II-b scheelite.

Apatite in the Stage I veinlets has comparable trace element compositions to the magmatic apatite. Both of these apatites have MREE-enriched patterns with pronounced negative Eu anomalies (Eu_N/Eu_N^* = 0.07–0.23 and 0.05, respectively; Fig. 8) and high ΣREE (2530–4310 and 3190 ppm, respectively), Mn (1370–1930 and 2270 ppm, respectively), and Fe (409–1170 and 1080 ppm, respectively), but low Sr contents (79.7–128 and 44.8 ppm, respectively)

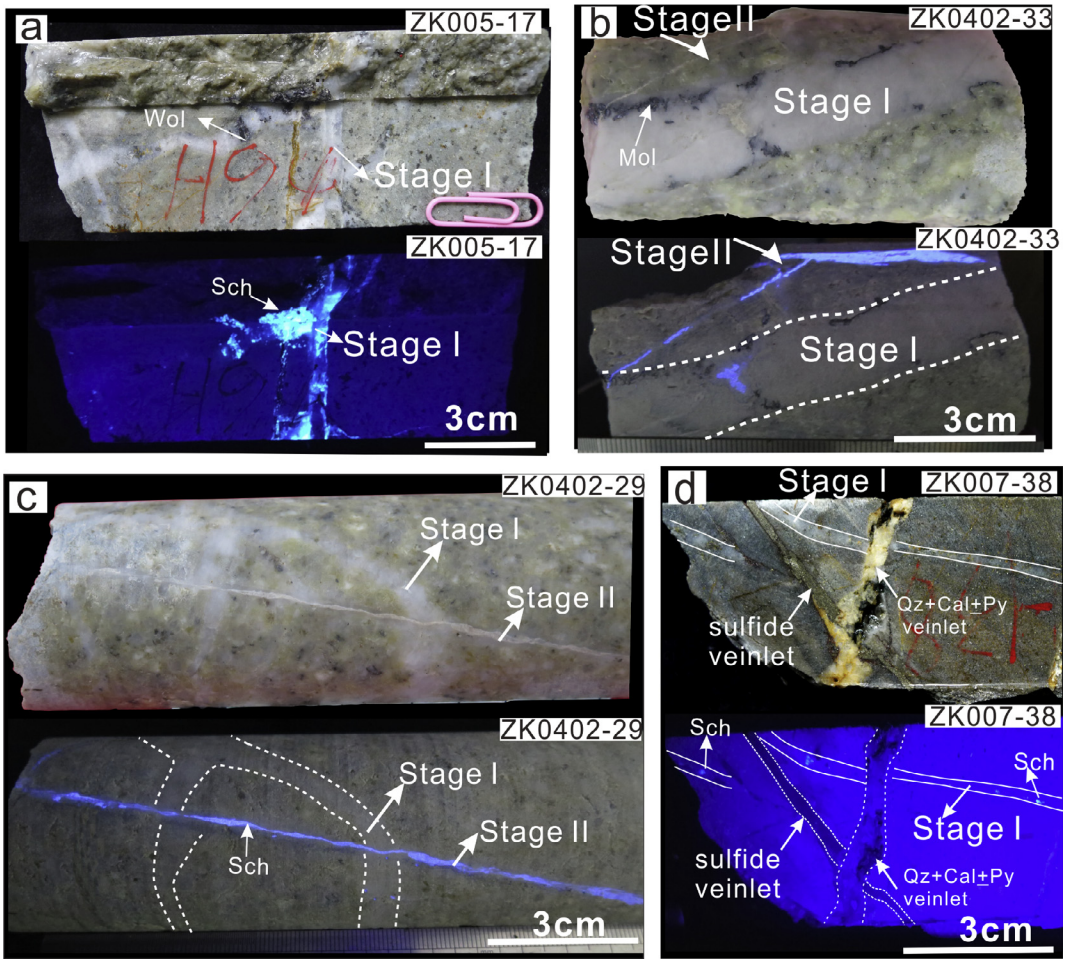

Fig. 4. Photographs of specimens showing crosscutting relationships of the scheelite-bearing and post-ore veinlets in the Muguayuan W deposit. (a): Scheelite ± wolframite ± molybdenite + quartz veinlet (Stage I). (b): Stage I veinlet is cut by scheelite + quartz + sericite veinlet (Stage II); molybdenite occurs at the sidewalls of the Stage I veinlet. (c): Stage II veinlet cuts Stage I veinlet. (d): Quartz + calcite ± pyrite veinlet cuts Stage I veinlet and sulfide veinlet; sulfide veinlet shifts Stage I veinlet. Abbreviations: Mol: molybdenite, Sch: scheelite, Wol: wolframite.

(Table 2). Compared with Stage I apatite, apatite in Stage II veinlets has LREE-enriched patterns with moderately negative Eu anomalies (Eu_N/Eu_N^* = 0.48–0.52; Fig. 8) and is relatively depleted in ΣREE (529–2230 ppm), Mn (111–158 ppm), and Fe (2.26–41.8 ppm), and enriched in Sr (2170–4690 ppm) (Table 2). Apatite in Stage II veinlets may have formed in two generations. One is intergrown with Stage II-a scheelite (Figs. 5g–h and 6c) and is considered to have formed synchronously with Stage II-a scheelite. The second is present interstitially between Stage II scheelite and quartz (Fig. 5i), and is thus assumed to have formed later (Stage II-b). Stage II-a apatite has higher ΣREE (2120–2230 ppm) than Stage II-b apatite (529 ppm) (Table 2).

6. Discussion

6.1. Source, nature, and evolution of ore-forming fluids

6.1.1. Stage I mineralization: reduced magma-derived fluids

Stage I veinlets comprise mainly scheelite, wolframite, quartz, and muscovite, and are associated with greisenization, which are indicative of a high-temperature hydrothermal system (Schwartz and Surjono,1990; Shapovalov and Setkova, 2012). The fluids responsible for greisenization are considered to be magma-derived (Korges et al., 2018; Somarin and Ashley, 2004; Webster et al., 2004), and inherit the REE patterns of the parent granite (e.g., negative Eu anomalies; Štemprok et al., 2005). Hydrothermal minerals from ore-forming fluids with different compositions will have distinctive REE compositions and patterns (Brugger et al., 2000; Ghaderi et al., 1999; Song et al., 2014). As such, REE features of hydrothermal mineral can be used to trace the origins of fluids (Linnen et al., 2014; Smith et al., 2004; Sun and Chen, 2017; Zhao et al., 2018). Magmatic and Stage I apatites have similar REE patterns (Fig. 8), suggesting a genetic link between these apatites. Stage I-a scheelite has LREE-enriched patterns and negative Eu anomalies, which resemble those of the granitic porphyry (Fig. 7a) and are indicative of a genetic link to the granite (Sun and Chen, 2017). These features indicate that the ore-forming fluids in Stage I were derived from granitic magma.

Europium is a variable valence element that exists as Eu^{3+} in an oxidized environment and Eu^{2+} under reduced conditions. Eu^{3+} has a similar partition coefficient between scheelite and fluids to other REE^{3+}, whereas the partition coefficient of Eu^{2+} is much lower (Brugger et al., 2000). Therefore, in the plot of chondrite-normalized Eu (Eu_N) versus Eu_N^* ($Eu_N^* = (Sm_N \times Gd_N)^{1/2}$) shown in Fig. 10, data for scheelite from Eu^{2+}-dominant fluids will plot parallel to the x-axis, whereas data for scheelite from oxidized fluids (Eu^{3+}-dominant) will plot along a line with a slope of one (Ghaderi et al., 1999). Data for Stage I scheelite forms a nearly horizontal line (Fig. 10), suggesting that Eu was predominantly Eu^{2+} in the Stage I fluids. Manganese in apatite is a reliable redox proxy, given that Mn contents in apatite show a negative correlation with oxygen fugacity (Miles et al., 2014). Magmatic and Stage I apatites have elevated Mn contents (2270 and 1370–1930 ppm, respectively), which confirm that the granitic porphyry and Stage I fluids were relatively reduced.

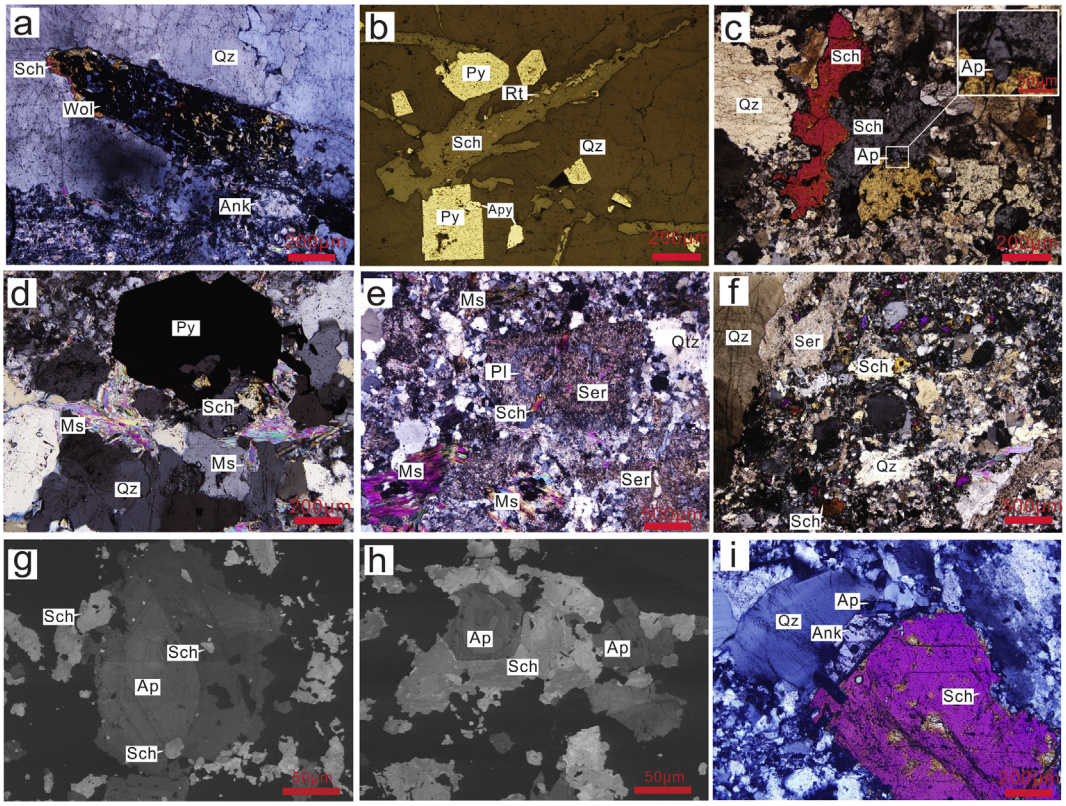

Fig. 5. Photomicrographs and cathodoluminescence images showing the occurrences of scheelite and apatite. (a) Wolframite is replaced by scheelite in Stage I veinlet (crossed polars, ZK006-20). (b) Disseminated euhedral pyrite and arsenopyrite in Stage I veinlet; rutile is associated with scheelite (reflected light, ZK006-20). (c) Scheelite occurs as aggregate in Stage I veinlet; apatite occurs as interstitial in scheelite (crossed polars, ZK006-39). (d) Muscovite occurs as aggregates and is associated with scheelite in Stage I veinlet (crossed polars, ZK006-20). (e) Disseminated scheelite grains occur in altered granite porphyry; note that phyllic alteration overprints the greisenization (crossed polars, Zk0402-41). (f) Anhedral scheelite is associated with quartz and sericite in Stage II veinlet (crossed polars, ZK0402-36). (g) Small scheelite grains are enclosed in apatite of the Stage II veinlet (CL image, ZK0402-36). (h) Apatite intergrows with the scheelite grain in stage II veinlet (CL image, ZK0402-36). (i) Scheelite occurs as megacryst in Stage II veinlet; ankerite and apatite are interstitial among the quartz and scheelite grains (crossed polars, ZK0402-33). Apatites present in c, g, h and i are selected to conduct in-situ LA-ICP-MS analyses, and the data are given in Table 2. Abbreviations: Ank: ankerite, Ap: apatite, Apy: arsenopyrite, Kfs: K-feldspar, Mol: molybdenite, Ms: muscovite, Pl: plagioclase, Py: pyrite, Qz: quartz, Rt: rutile, Sch: scheelite, Ser: sericite, Wol: wolframite.

Molybdenum and manganese in exsolved fluids tend to increase during the progressive crystallization of granitic magma (Audetat and Pettke, 2003). Stage I scheelite has elevated Mo and Mn contents (Fig. 9a), which suggests that the Stage I fluids were Mo–Mn-enriched. The occurrence of molybdenite in Stage I veinlets also indicates the Mo-rich nature of the Stage I ore-forming fluids. Strontium is a compatible element in apatite (Prowatke and Klemme, 2006). As such, Sr in apatite is controlled mainly by the Sr content of the fluid or melt from which the apatite forms. Both the magmatic and Stage I apatites have relatively low Sr contents (44.8 and 79.7–127 ppm, respectively; Table 2), indicating that the granitic melt and its exsolved fluids were Sr-poor. The Sr contents in Stage I scheelite are also low (37.7–487 ppm; Fig. 9d; Table 1), reflecting the Sr-poor nature of the Stage I fluids.

Although Stage I-b scheelite has low REE concentrations and positive Eu anomalies, which differ from Stage I-a scheelite, both I-a and I-b scheelites have similar LREE-enriched patterns. This suggests that the Stage I-b fluids were derived from the Stage I-a fluids. Minerals that precipitated from Stage I-a fluids, as well as fluid–rock interaction (greisenization), likely changed the fluid composition from Stages I-a to I-b. The precipitation of REE-rich apatite and Stage I-a scheelite would have removed REEs from the fluids, resulting in a relative depletion of REEs in the evolved fluids and, as such, in Stage I-b scheelite. The decomposition of plagioclase during greisenization would have also released Eu and Sr into the fluids, which may have been responsible for the elevated Eu and Sr contents (Fig. 9d) and positive Eu anomalies in Stage I-b scheelite (Fig. 7a–b and d).

6.1.2. Stage II mineralization: involvement of oxidized meteoric water

Unlike Stage I mineralization that was associated with greisenization, Stage II mineralization was closely related to phyllic alteration. Phyllic alteration typically overlaps greisenization in W-(Sn) ore deposits (Heinrich, 1990; Pirajno, 2009; Štemprok et al., 2005), and is conventionally thought to result from interaction with evolved fluids formed by the mixing of magmatic fluids and low-temperature meteoric water (Reynolds and Beane, 1985; Taylor, 1974, 1997). Thus, the fluids of Stage II were evolved and had different compositions and physicochemical conditions from the magmatic fluids of Stage I.

Of note, the Sr concentration of Stage II scheelite is more than one order of magnitude higher than that of Stage I scheelite (Fig. 9d). Stage II apatite also has elevated Sr contents. Thus, the Stage II fluids likely had much higher Sr contents than the Stage I fluids. Strontium is compatible in both scheelite and apatite (Brugger et al., 2000; Prowatke and Klemme, 2006), meaning that the precipitation of Stage I scheelite and apatite would have lowered rather than increased the fluid Sr content. Differentiation of magma also cannot elevate the Sr content of exsolved fluids (Bai and Groos, 1999; Chappell and White, 1992). Therefore, an extra source of Sr is required to account for the formation of Sr-rich scheelite in Stage II. Strontium-rich scheelite (1455–6810 ppm) is also found in the Woxi deposit (Fig. 1b), where high-Sr fluid is thought to have resulted from the hydrothermal leaching of Proterozoic strata (Peng et al., 2003). The strata in the Muguayuan W deposit are mainly part of the Neoproterozoic Banxi and Lengjiaxi groups (Fig. 2a), which contain pyroclastic and tholeiitic to

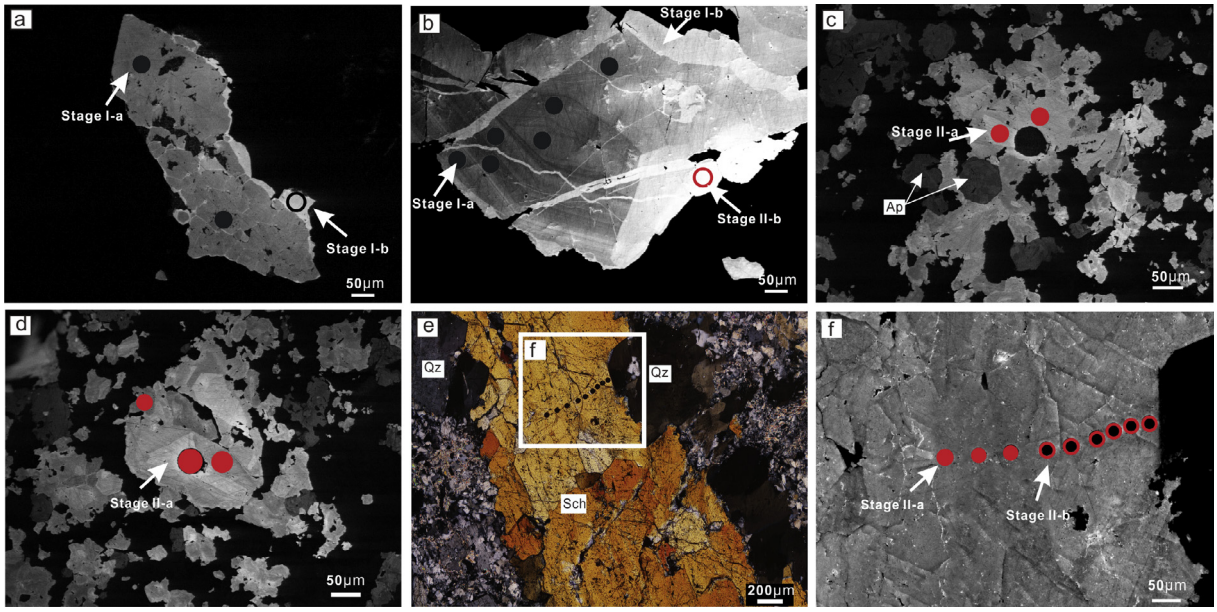

Fig. 6. Representative cathodoluminescence images and photomicrograph of scheelites. (a) Disseminated scheelite in altered granite porphyry (ZK0402-41), showing similar texture with that of scheelite from Stage I veinlet (b). (b) Scheelite from Stage I veinlet; Stage I-a scheelite in dark domains has oscillatory zone and Stage I-b scheelite occurs as bright overgrowth of inner dark CL domains; Stage II-b scheelite occurs as overgrowth at the rim and as micro-veinlet penetrating the Stage I scheelite (ZK006-39). (c–d) Scheelites from Stage II veinlet without obvious zoning in CL images (ZK0402-36). (e) Photomicrograph of a scheelite megacryst from Stage II veinlet; the dark spots in the scheelite represent laser ablation pits (crossed polars, ZK0402-33). (f) CL image of the scheelite in the box in Fig. 6e. Circles in the CL images represent laser ablation pits. Abbreviations of minerals are the same as Fig. 5.

calc-alkaline volcanic rocks (He and Han, 1992; Wang et al., 2004; Wang et al., 2007a,b; Xiao, 1983). These mafic-intermediate volcanic and pyroclastic rocks are Sr-rich (Wang et al., 2004), and possibly provided the extra Sr in the Stage II fluids through interactions with meteoric water. The mixing of magmatic fluids with meteoric waters in the late stages of W (and Sn) mineralization has also been proposed for other W ore deposits. For example, Pollard et al. (1991) hypothesized that dissipation of a magmatic hydrothermal system would facilitate the involvement of meteoric water in the mineralization system. Somarin and Ashley (2004) also suggested that with decreasing temperature, meteoric waters would be introduced and mixed with magmatic fluids, which triggered the low-temperature alteration and late-stage ore mineral precipitation in the Glen Eden Mo–W–Sn deposit, Australia. Wang et al. (2015) analyzed the H–O isotopic compositions of fluid inclusions in the Dahutang deposit, and suggested that the early ore-forming fluids were magma-derived, and were then progressively mixed with meteoric water during later mineralization stages.

The influx of meteoric water would have increased the oxygen fugacity of Stage II fluids, given that meteoric water is usually more oxidized than magmatic fluids (White, 1955). Stage II apatite has very low Mn contents (111–158 ppm) that are indicative of relatively oxidized conditions (Miles et al., 2014). In Fig. 10, data for the Stage II scheelites plot broadly along a diagonal array, which suggests that Eu in the fluid of this stage was dominantly Eu^{3+} (Ghaderi et al., 1999). This supports the inference that Stage II fluids were relatively oxidized as compared with Stage I.

From Stages I to II, scheelite Mo, Mn, Nb, and Ta contents show a nearly linear change (Fig. 9a–b), which might have been caused by the successive precipitation of hydrothermal minerals (Song et al., 2014; Zhao et al., 2018). Crystallization of molybdenite during Stage I would have significantly depleted the fluid Mo content, whereas the precipitation of Stage I oxides (e.g., rutile; Green, 1995) and Nb-Ta-rich scheelite would have removed Nb and Ta from the fluids. Stage I scheelite is LREE- and Mn-rich, and Stage I apatite is REE- and Mn-rich. The precipitation of these minerals would have lowered the REE (particularly LREE) and Mn contents of the remaining fluids. Stage II-a apatite is LREE-rich (Fig. 8) and would have depleted the LREEs in the Stage II fluids. Therefore, the Stage II ore-forming fluids have relatively low Mo, Mn, Nb, Ta, and REE (particularly LREE) contents, which are recorded by the Stage II-a scheelite (Figs. 7e–f and 9a–c; Table 1).

6.2. Modeling REE variations during scheelite precipitation

We modeled the REE compositional variations of scheelite and fluids during the precipitation of scheelite in the Muguayuan W deposit using the batch crystallization model. We assumed the initial fluid/scheelite ratio (R_1) is

$$R_1 = M_{f1}/M_{m1} \quad (1)$$

where M_{f1} and M_{m1} are the mass fractions of fluid and scheelite in the first crystallization batch, respectively. The partition coefficient (D) is

$$D = C_m/C_f \quad (2)$$

where C_m and C_f are the concentrations of REEs in the scheelite and fluid, respectively. In these calculations, we assumed that the partition coefficients between scheelite and fluid remained constant. The REE content in the initial fluid (C_0) can be calculated as follows:

$$C_0 = (C_{f1} \times M_{f1} + C_{m1} \times M_{m1})/(M_{f1} + M_{m1}) \quad (3)$$

where C_{m1} and C_{f1} are the REE concentrations in the scheelite and fluid of the first crystallization batch, respectively. Combining Eqs. (1)–(3) yields

$$C_0 = C_{m1} \times (R_1+D)/(1 + R_1)/D \quad (4)$$

In the first batch of scheelite precipitation (termed 1th Sch), Eq. (4) leads to

$$C_{m1} = C_0 \times (1 + R_1) \times D/(R_1+D) \quad (5)$$

$$C_{f1} = C_{m1}/D \quad (6)$$

During the 2nd Sch, we set $R_2 = R_1 - 1$, which reflects the decrease in the fluid mass fraction in the fluid-scheelite system due to the crystal fractionation during the 1th Sch. This then leads to

$$C_{m2} = C_{f1} \times (1 + R_2) \times D/(R_2+D) \quad (7)$$

Table 1
LA-ICP-MS analyses of trace elements (in ppm) of scheelite from the Muguayuan W deposit.

Stage	Stage I-a															
Sample	ZK006-34						ZK006-20							ZK006-39		
Spot	1	5	6	7	8	3	7	8	1	2	3	16	18	4	7	9
La	326	606	206	436	168	313	377	138	230	239	292	80.6	55.7	165	239	276
Ce	549	1520	554	1090	477	742	806	357	517	515	589	149	105	321	523	555
Pr	57.0	206	78.3	149	68.5	99.1	90.9	46.9	60.4	60.7	66.6	16.0	11.3	39.8	60.6	59.0
Nd	198	947	354	689	310	454	342	206	238	231	255	48.3	43.2	171	225	201
Sm	35.9	210	101	129	92.4	114	70.9	63.2	61.2	49.7	50.0	12.2	11.3	55.3	46.8	37.8
Eu	9.95	8.72	4.10	8.14	6.28	7.32	8.41	6.13	9.55	9.60	6.42	2.97	1.57	10.7	3.65	5.20
Gd	28.2	186	105	99.1	102	115	62.6	91.1	75.6	45.2	40.2	10.6	11.0	65.9	37.1	32.0
Tb	4.48	25.8	17.7	11.7	18.3	17.8	10.5	19.2	14.9	7.51	5.77	2.25	2.19	11.8	5.88	5.36
Dy	26.3	144	109	60.9	120	109	67.7	142	100	48.7	33.0	15.2	14.5	74.7	32.8	34.5
Ho	5.47	26.4	21.1	11.3	23.9	21.6	13.3	29.9	19.9	9.39	5.82	3.20	3.09	14.0	5.97	6.54
Er	15.8	67.4	52.8	26.4	61.9	55.4	36.6	79.8	53.6	25.0	15.0	9.61	10.3	35.2	15.6	18.1
Tm	2.44	8.68	6.94	3.49	8.37	7.69	5.38	10.6	7.91	3.69	1.87	1.84	1.76	4.57	2.02	2.87
Yb	18.7	55.3	40.1	22.3	50.2	47.1	38.5	63.2	47.2	24.7	11.3	13.7	13.3	23.6	13.0	20.0
Lu	2.98	6.79	4.70	2.97	5.66	6.23	5.14	7.54	5.99	2.74	1.44	1.89	1.83	2.75	1.49	2.56
Y	141	605	467	257	560	477	373	762	519	248	152	106	81.8	304	164	191
ΣREE	1280	4020	1650	2740	1510	2110	1940	1260	1440	1270	1370	367	285	995	1210	1260
Eu_N/Eu_N^*	0.96	0.13	0.12	0.22	0.20	0.20	0.39	0.25	0.43	0.62	0.44	0.80	0.43	0.54	0.27	0.46
$(La/Sm)_N$	5.85	1.86	1.32	2.19	1.17	1.77	3.44	1.40	2.43	3.10	3.77	4.26	3.20	1.92	3.29	4.71
$(La/Yb)_N$	12.5	7.86	3.69	14.0	2.40	4.76	7.04	1.56	3.49	6.94	18.5	4.21	3.00	5.01	13.1	9.87
Mn	106	91.1	93.2	75.8	78.3	99.1	84.5	78.3	80.6	71.3	58.7	115	244	65.5	69.4	69.3
Sr	54.0	48.6	48.5	59.5	46.0	52.2	53.1	40.8	51.8	58.7	59.0	46.0	52.8	313	49.4	37.7
Nb	67.8	252	165	121	157	144	148	121	155	83.0	96.4	117	85.1	88.8	130	148
Mo	762	2010	741	1310	247	943	925	189	363	337	543	436	453	738	1920	1610
Ta	2.01	11.0	5.83	4.04	5.06	6.23	8.92	10.4	8.73	4.65	5.62	1.91	2.94	3.15	3.35	4.10

Stage	Stage I-a										Stage I-b				
Sample	ZK006-39			ZK0402-41							ZK0402-41		ZK006-34		ZK006-20
Spot	1	11	12	3	4	11	7	9	15	1	8	2	2	4	9
La	278	241	173	326	120	362	117	255	225	284	170	171	180	132	45.1
Ce	546	624	515	664	264	759	299	645	546	572	281	362	304	225	76.6
Pr	57.5	82.5	66.5	76.5	32.7	73.7	39.4	74.7	59.6	65.6	23.5	43.1	32.9	22.3	8.31
Nd	193	354	294	298	131	287	161	312	225	252	69.3	188	126	77.5	30.6
Sm	38.4	106	93.1	69.8	31.3	62.5	44.1	84.5	55.7	52.3	13.0	55.3	21.1	11.5	7.71
Eu	6.55	7.81	9.45	8.17	5.03	5.08	4.58	9.00	8.59	3.09	6.63	22.8	8.11	5.08	22.9
Gd	30.2	114	110	64.4	29.9	63.6	43.3	90.0	58.0	47.6	12.1	62.7	15.0	7.10	9.47
Tb	5.39	22.4	20.1	10.92	5.13	10.6	8.35	15.4	10.1	7.86	2.11	9.00	1.96	0.88	1.94
Dy	36.0	140	135	68.7	31.9	64.7	52.8	98.6	61.2	50.4	13.8	51.0	9.65	4.77	11.1
Ho	6.90	28.3	26.7	13.7	6.44	12.7	10.6	19.6	11.3	10.00	2.98	8.96	1.66	0.73	2.17
Er	20.3	73.4	67.9	36.1	16.3	33.9	28.9	54.2	29.1	27.8	8.08	21.0	4.85	2.68	5.87
Tm	3.36	9.85	9.38	4.99	2.27	4.81	4.22	7.83	4.14	3.94	1.25	2.80	0.70	0.24	1.08
Yb	23.0	54.9	52.2	32.0	14.1	32.6	25.0	50.8	30.5	25.6	9.15	16.2	5.24	2.79	7.30
Lu	2.87	6.74	6.29	4.11	1.75	4.02	3.04	6.08	3.80	3.40	1.10	1.81	0.76	0.35	1.08
Y	196	666	626	343	160	283	266	410	290	250	88.5	194	44.1	22.1	64.0
ΣREE	1250	1860	1580	1680	691	1780	841	1720	1330	1410	613	1020	712	493	231
Eu_N/Eu_N^*	0.59	0.22	0.29	0.37	0.50	0.25	0.32	0.32	0.46	0.19	1.62	1.18	1.40	1.72	8.20
$(La/Sm)_N$	4.68	1.47	1.20	3.01	2.48	3.74	1.71	1.95	2.60	3.50	8.43	2.00	5.52	7.43	3.78
$(La/Yb)_N$	8.68	3.15	2.37	7.29	6.11	7.97	3.36	3.60	5.28	7.95	13.3	7.60	24.7	34.0	4.43
Mn	78.7	75.4	75.1	93.6	127	79.4	67.8	112	101	99.47	126	61.7	112	103	48.1
Sr	44.5	41.2	96.7	58.8	150	58.8	62.1	72.75	237	43.03	71.0	487	61.1	59.8	166
Nb	142	266	172	104	188	45.9	42.6	140	105	159	21.8	75.9	39.1	30.7	71.1
Mo	3420	1570	486	969	2110	490	387	680	3160	1500	518	1040	876	2880	3.63
Ta	5.71	9.57	6.12	3.23	5.14	1.23	0.87	3.30	2.95	4.61	0.36	2.16	1.38	1.00	0.49

Stage	Stage II-a													Stage II-b	
Sample	ZK0402-33							ZK006-20		ZK0402-36				ZK006-39	ZK0402-33
Spot	3	15	16	19	2	21	22	5	19	2	3	4	5	9	13	1
La	22.3	9.50	25.8	32.1	26.9	24.3	32.2	11.6	88.7	13.9	13.9	15.9	69.0	18.6	71.9	14.0
Ce	116	64.0	85.2	172	104	95.1	144	58.8	305	49.1	94.7	104	290	51.5	77.5	10.6
Pr	20.7	15.3	12.3	30.1	16.6	13.1	20.8	16.1	47.7	10.2	23.0	25.0	45.7	8.63	5.60	0.66
Nd	102	102	53.3	136	78.2	50.0	84.4	113	241	49.1	150	143	204	40.1	14.0	1.51
Sm	50.1	68.1	21.3	58.1	38.5	17.3	33.5	96.0	90.2	24.5	90.0	74.5	89.0	18.9	2.88	0.24
Eu	11.1	10.5	6.65	14.8	7.36	5.87	8.77	36.9	10.0	5.44	15.8	13.7	23.3	4.12	8.38	0.35
Gd	67.7	84.6	30.7	83.5	48.7	23.6	47.1	135	138	38.5	114	103	132	25.6	2.74	0.37
Tb	12.7	14.8	7.15	19.3	9.63	4.79	10.0	23.3	28.6	8.96	22.4	22.2	32.3	5.76	0.68	0.08

(*continued on next page*)

Table 1 (*continued*)

Stage	Stage II-a														Stage II-b	
Sample	ZK0402-33							ZK006-20		ZK0402-36					ZK006-39	ZK0402-33
Spot	3	15	16	19	2	21	22	5	19	2	3	4	5	9	13	1
Dy	80.2	72.5	48.7	130	57.1	33.8	68.1	110	198	57.7	128	134	235	39.3	6.21	1.32
Ho	14.7	10.1	9.98	24.9	10.2	7.18	14.2	14.9	42.5	10.8	20.4	22.7	50.7	7.27	1.50	0.45
Er	35.1	19.5	27.9	62.8	24.6	20.2	37.1	27.4	111	23.8	39.7	47.3	132	18.6	6.31	1.82
Tm	4.32	1.95	3.76	7.13	3.18	3.05	4.78	2.64	14.2	2.75	4.02	4.95	17.2	2.58	1.57	0.58
Yb	22.1	7.80	22.7	34.3	18.4	17.7	25.5	13.1	77.5	13.7	17.0	18.9	90.6	15.9	17.7	6.83
Lu	2.07	0.67	2.46	3.09	1.98	1.91	2.55	1.23	9.14	1.66	1.33	1.60	9.31	2.13	3.12	1.38
Y	287	150	226	476	233	217	296	242	913	164	269	315	969	161	54.7	36.9
ΣREE	560	482	358	807	446	318	533	660	140	310	734	730	1420	259	220	40.1
Eu_N/Eu_N^*	0.58	0.42	0.79	0.65	0.52	0.89	0.68	0.99	0.27	0.54	0.48	0.48	0.66	0.57	9.12	3.61
$(La/Sm)_N$	0.29	0.09	0.78	0.36	0.45	0.90	0.62	0.08	0.63	0.37	0.10	0.14	0.50	0.63	2.00	37.9
$(La/Yb)_N$	0.72	0.87	0.81	0.67	1.05	0.99	0.91	0.64	0.82	0.73	0.59	0.60	0.55	0.84	7.60	1.47
Mn	2.90	1.79	5.48	3.94	1.89	2.12	2.04	0.47	38.7	10.9	4.30	7.09	2.58	15.0	77.3	5.62
Sr	1500	1470	2520	1870	1670	1550	1800	1650	108	1930	1390	1570	1650	2780	60.3	2540
Nb	16.9	16.4	8.52	14.1	6.02	8.91	10.6	4.51	154	8.15	14.7	13.3	11.0	7.92	19.8	2.66
Mo	b.d.	0.09	13.85	0.14	1.89	0.13	0.29	0.06	1.23	0.19	0.04	0.24	0.08	0.10	71.1	0.19
Ta	0.16	0.18	0.11	0.19	0.08	0.09	0.14	0.06	2.50	0.25	0.38	0.28	0.29	0.24	0.61	0.08

Stage	Stage II-b													
Sample	ZK0402-33													
Spot	2	4	5	6	7	8	9	10	11	12	13	14	17	18
La	43.2	28.9	18.4	24.1	32.6	27.7	19.7	23.3	13.1	7.72	9.93	10.2	16.3	13.4
Ce	121	93.1	14.6	28.6	48.1	38.3	17.5	26.4	15.6	5.69	8.84	9.09	12.3	24.5
Pr	12.2	10.3	0.82	2.24	3.94	3.04	1.01	1.67	1.16	0.31	0.75	0.54	0.89	2.25
Nd	35.7	31.4	1.73	5.89	10.8	8.91	2.41	4.68	3.26	0.68	2.69	0.97	3.36	6.96
Sm	9.41	8.28	0.48	1.25	2.33	1.87	0.42	0.83	0.74	0.15	0.99	0.25	1.54	1.56
Eu	5.54	3.97	0.20	0.56	0.92	0.88	0.22	0.45	0.75	0.22	0.49	0.37	0.48	0.90
Gd	13.0	11.7	0.70	2.23	4.13	3.64	0.70	1.46	1.23	0.22	1.42	0.39	1.83	1.71
Tb	3.00	2.88	0.14	0.54	0.98	0.87	0.20	0.36	0.35	0.07	0.28	0.11	0.38	0.40
Dy	26.8	24.0	1.34	4.61	8.76	7.59	1.79	3.41	3.23	0.79	2.15	1.25	2.33	3.60
Ho	7.27	6.09	0.39	1.21	2.59	1.90	0.48	0.99	0.85	0.24	0.47	0.41	0.42	0.89
Er	25.7	19.9	2.02	4.62	10.4	6.84	2.33	4.16	3.44	1.12	2.00	1.90	1.62	3.61
Tm	4.39	3.36	0.53	1.08	2.05	1.47	0.62	0.90	0.74	0.38	0.50	0.56	0.48	0.70
Yb	30.4	20.4	6.63	9.77	17.6	12.1	7.01	9.32	7.19	4.74	5.82	6.21	6.70	7.10
Lu	3.39	2.39	1.14	1.60	2.49	1.96	1.30	1.56	1.17	0.82	0.92	1.04	1.23	1.09
Y	280	217	31.5	64.5	105	90.4	36.6	59.6	48.1	22.9	30.0	36.6	32.2	54.9
ΣREE	341	267	49.1	88.4	148	117	55.7	79.6	52.8	23.2	37.2	33.3	49.9	68.7
Eu_N/Eu_N^*	1.53	1.23	1.08	1.03	0.91	1.03	1.24	1.24	2.42	3.59	1.27	3.70	0.87	1.68
$(La/Sm)_N$	2.96	2.25	24.9	12.5	9.02	9.52	30.6	18.2	11.4	32.5	6.50	26.8	6.83	5.56
$(La/Yb)_N$	1.02	1.02	1.99	1.77	1.33	1.64	2.02	1.80	1.30	1.17	1.23	1.18	1.75	1.35
Mn	2.03	2.75	3.89	3.90	4.17	4.64	4.64	6.89	4.72	10.6	7.10	4.64	4.63	4.20
Sr	1810	1470	1950	2170	2060	1990	1990	2060	2640	2780	2710	2270	3080	2340
Nb	4.75	5.90	2.86	2.59	3.00	3.35	2.66	3.18	2.75	3.80	2.91	2.79	3.85	3.03
Mo	0.07	0.08	0.06	0.11	0.06	0.03	1.86	0.18	0.06	0.09	0.10	0.05	2.32	0.07
Ta	0.10	0.09	0.06	0.06	0.06	0.07	0.06	0.07	0.07	0.10	0.06	0.07	0.08	0.07

Note: b.d.-below detection limit.

$$C_{f2} = C_{m2}/D \quad (8)$$

During the nth Sch (n is a positive integer), we set $R_n = R_{1-n} + 1$, which leads to

$$C_{mn} = C_{fn-1} \times (1 + R_n) \times D/(R_n+D) \quad (9)$$

$$C_{fn} = C_{mn}/D \quad (10)$$

The REE partition coefficients between scheelite and fluid were taken from Brugger et al. (2000). Due to the very different partition coefficients of Eu^{2+} and Eu^{3+}, the bulk partition coefficient of Eu^{2+} and Eu^{3+} is defined as D_{Eu}, which can be calculated as

$$D_{Eu} = F\times D_{Eu2+} + (1-F) \times D_{Eu3+} \quad (11)$$

where F is the mass fraction of Eu^{2+} in the initial fluid.

The Stage I and II fluids had different oxygen fugacities, meaning that their Eu^{2+}/Eu^{3+} ratios were different. Values of F = 0.85 and F = 0.4 were assumed for Stages I and II, respectively. This is consistent with the inference that Stage I and II fluids were Eu^{2+}- and Eu^{3+}-dominant, respectively (Fig. 10).

For Stage I, we choose sample ZK006-34, which has relatively continuous and variable scheelite REE contents, to model the REE fractionation during scheelite precipitation. The initial fluid/scheelite ratio (R_1) was set to 120, and the REE concentration of the system was calculated from Eq. (4) using the REE concentration of analysis 5 in sample ZK006-34, which had the highest measured REE concentration and thus may be most representative of the initial fluid (Table 1). For Stage II, sample ZK0402-33 was selected to conduct the modeling. The initial fluid/scheelite ratio was set to 60 and C_{oREE} was based on analysis 19 in ZK0402-33, which had the highest measured REE concentration (Table 1). The modeling results are provided in Supplementary Table A1.

It should be noted that the natural scheelite-fluid system is more complex than the model we developed. For example, there are other REE-rich minerals, such as apatite, in the natural system, and scheelite-fluid REE partition coefficients may change as the system evolves. However, given that scheelite is the dominant REE-bearing mineral in the system, we use our simplified model. The similar measured and

Table 2
LA-ICP-MS analyses of trace elements (in ppm) of apatite from the Muguayuan W deposit.

Type	Magmatic apatite	Stage I apatite	Stage I apatite	Stage II-a apatite	Stage II-a apatite	Stage II-b apatite
Sample	ZK006-34-09	ZK006-20-20	ZK006-39-05	ZK0402-36-01	ZK0402-36-06	ZK0402-33-08
La	240	198	286	370	298	79.8
Ce	742	616	994	803	774	147
Pr	114	96.7	161	81.9	95.4	18.4
Nd	581	478	806	286	366	82.8
Sm	252	207	305	83.7	126	38.2
Eu	4.20	17.6	8.31	16.3	22.2	6.60
Gd	328	264	412	111	160	46.6
Tb	65.5	53.1	80.6	22.0	30.7	8.44
Dy	400	317	529	148	178	46.3
Ho	75.7	54.9	108	30.2	32.1	8.29
Er	189	123	291	77.4	77.7	18.7
Tm	25.3	15.2	40.1	10.5	9.78	2.76
Yb	153	78.3	253	67.6	57.3	21.6
Lu	20.0	8.33	32.5	8.80	7.30	3.13
Y	1920	1400	2950	934	838	267
ΣREE	3190	2530	4310	2120	2230	529
Eu_N/Eu_N^*	0.05	0.23	0.07	0.52	0.48	0.48
$(La/Sm)_N$	0.61	0.62	0.60	2.85	1.53	1.35
$(La/Yb)_N$	1.12	1.82	0.81	3.92	3.73	2.65
Mn	2270	1930	1370	156	158	111
Fe	1080	1170	409	41.8	34.5	2.26
Sr	44.8	79.7	128	2660	4690	2170

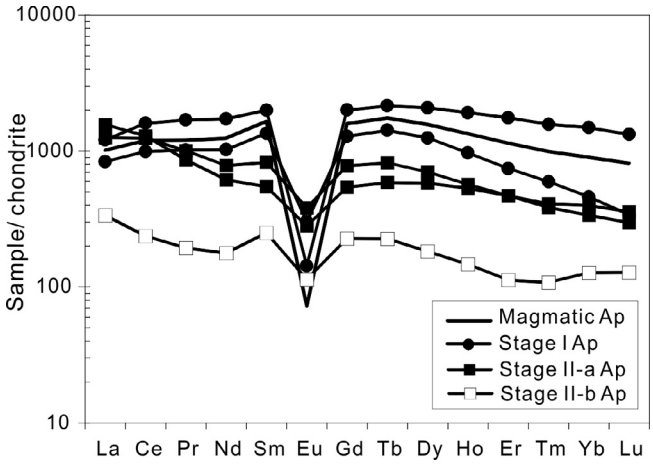

Fig. 8. Chondrite-normalized REE patterns of apatite from the Muguayuan W deposit. Chondrite values are from Sun and McDonough (1989).

modeled REE results indicate that our model is reliable (Fig. 11).

The modeling results support the inference that the Stage I and II fluids had different compositions and physicochemical conditions. The initial Stage I fluids were relatively reduced (Eu^{2+}-dominant) and had a similar REE pattern to that of the Sanxianba granitic porphyry (Fig. 11a), indicating that these fluids were exsolved from the granitic magma. Initial Stage II fluids were relatively oxidized and evolved, and

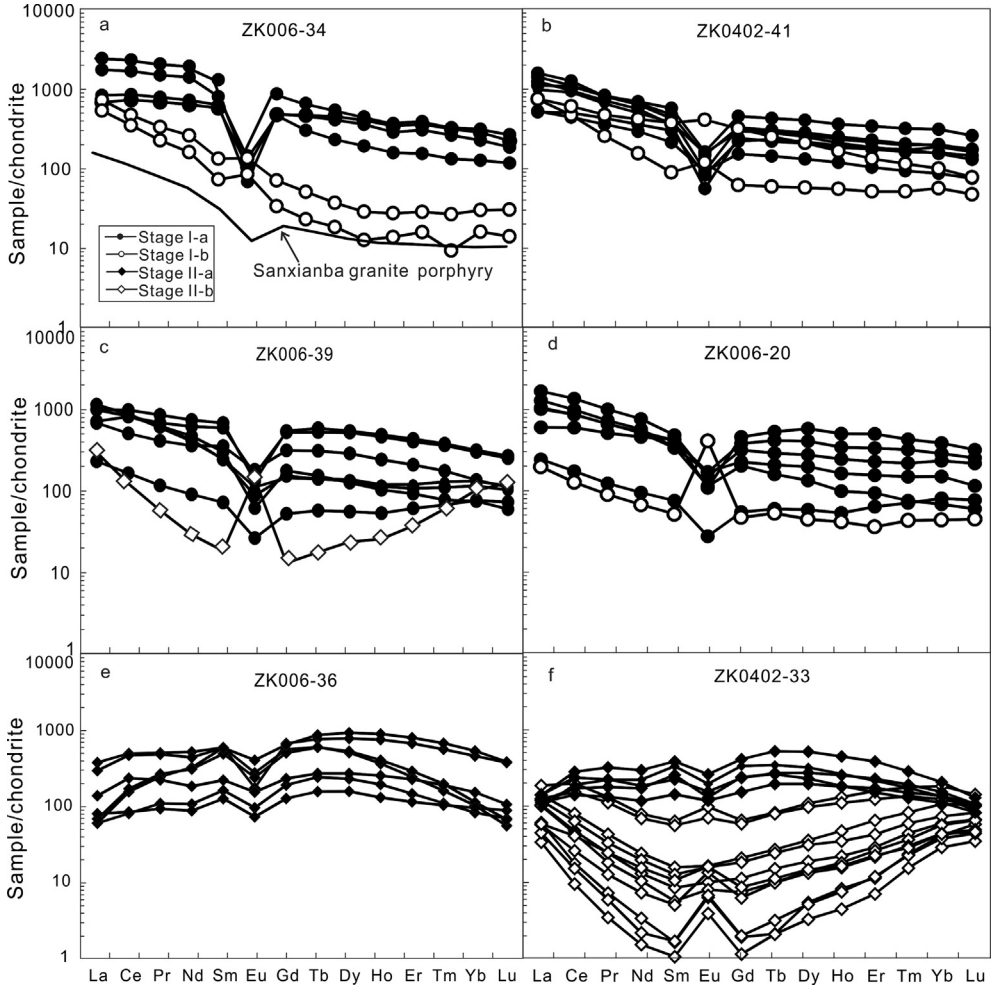

Fig. 7. Chondrite-normalized REE patterns of scheelites from the Muguayuan W deposit. Chondrite values are from Sun and McDonough (1989). REE concentration of Sanxianba granite porphyry is from our unpublished data.

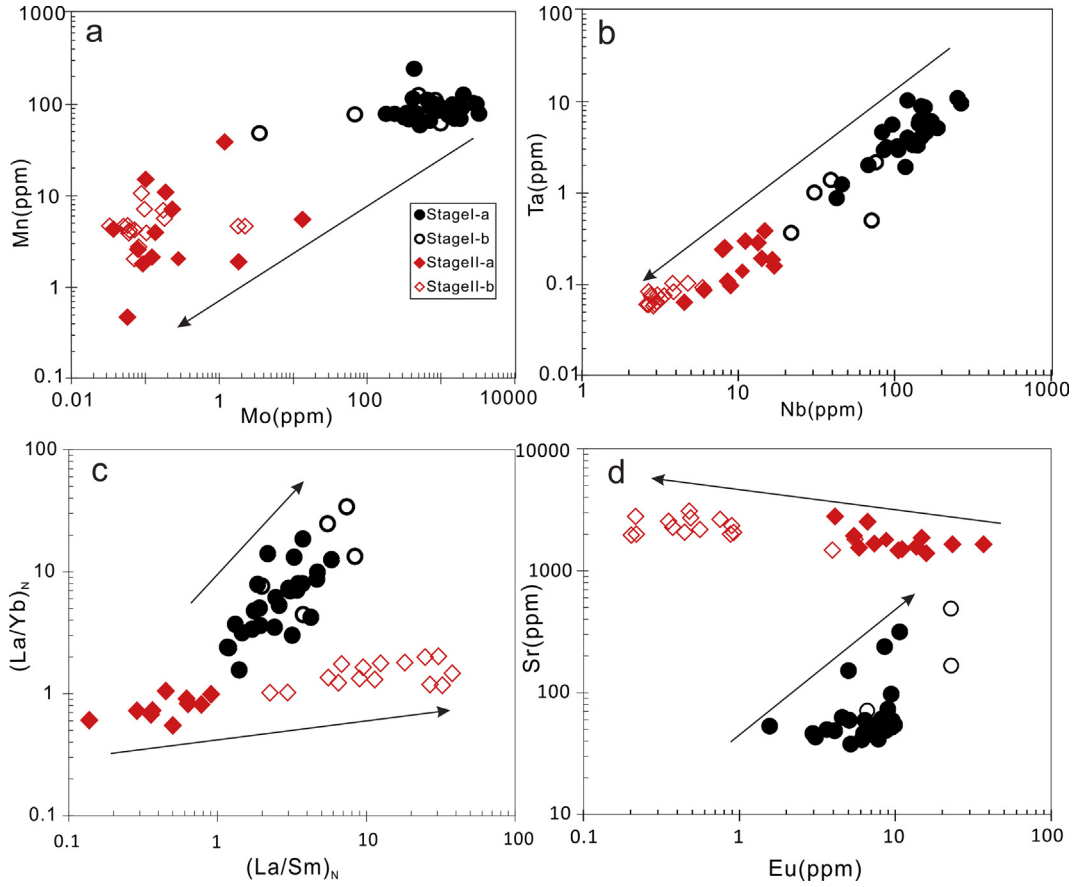

Fig. 9. Comparison of trace element compositions of different scheelites from the Muguayuan W deposit. (a): Mo VS. Mn; (b): Nb VS. Ta; (c): $(La/Sm)_N$ VS. $(La/Yb)_N$; (d): Eu VS. Sr. $(La/Sm)_N$ represents the fractionation among LREE and MREE, while $(La/Yb)_N$ represents fractionation among LREE and HREE, chondrite values are from Sun and McDonough (1989).

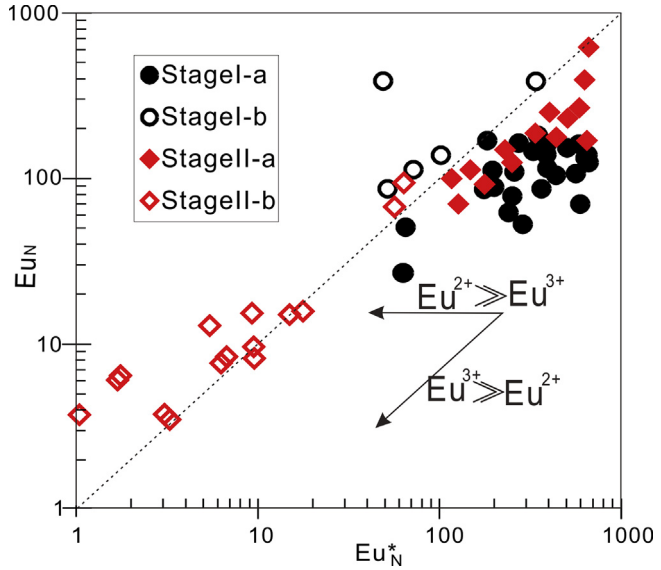

Fig. 10. Plot of chondrite-normalized Eu concentrations (Eu_N) vs. calculated Eu^*_N values of scheelite, where $Eu^*_N = (Sm_N * Gd_N)^{1/2}$. The dashed line represents 1:1 correlation line assuming that Eu_N is identical to Eu^*_N.

had relatively flat REE patterns (Fig. 11b). The previous precipitation of scheelite would have significantly changed the trace element chemistry of residual fluids and, as such, subsequently precipitated scheelite (Fig. 11). The modelling results also indicate that Stages I and II had different fluid/scheelite ratios. Stage I scheelite precipitated at relatively high fluid/scheelite ratios, whereas the fluid/scheelite ratios of Stage II were relatively low (Supplementary Table A1).

6.3. Genesis of the Muguayuan W deposit

The mechanism of W mineralization is an important field of research, but remains poorly understood (Korges et al., 2018; Štemprok and Seltmann, 1994). It is generally accepted that fluid exsolution is an important prerequisite for W migration and mineralization (Audetat et al., 2000a, 2000b; Manning and Henderson, 1984; Pirajno, 2009; Wood and Samson, 2000; Zajacz et al., 2008). The early fluids in granite-related W deposits are typically dominantly magma-derived, and become progressively mixed with meteoric waters in later stages (Audetat et al., 2000b; Beuchat et al., 2004; Bowman et al., 1985; Gao et al., 2014; Lu et al., 2003; Mangas and Arribas, 1988; Wang et al., 2017). Tungsten (and Sn) mineralization is commonly associated with extensive fluid-rock alteration (Esmaeily et al., 2005; Heinrich, 1990; Pollard, 1983; Somarin and Ashley, 2004; Štemprok, 1987; Štemprok et al., 2005; Webster et al., 2004), and it has been suggested that fluid-rock reaction is important (or essential) for the formation of W ore deposits (Jiang et al., 2015; Korges et al., 2018; Lecumberri-Sanchez et al., 2017; Pirajno, 2009).

The Muguayuan W deposit provides an excellent opportunity to better understand W mineralization. According to our observations, the mineralization in this deposit can be divided into two stages. In Stage I, the initial ore-forming fluids were magma-derived, relatively reduced, and had similar REE compositions to those of the Sanxianba granitic porphyry (Fig. 11a). The fluids caused extensive greisenization, during which biotite and feldspar were replaced by muscovite and sericite. The replacement of biotite by muscovite released Mn, Nb, and Ta into fluids

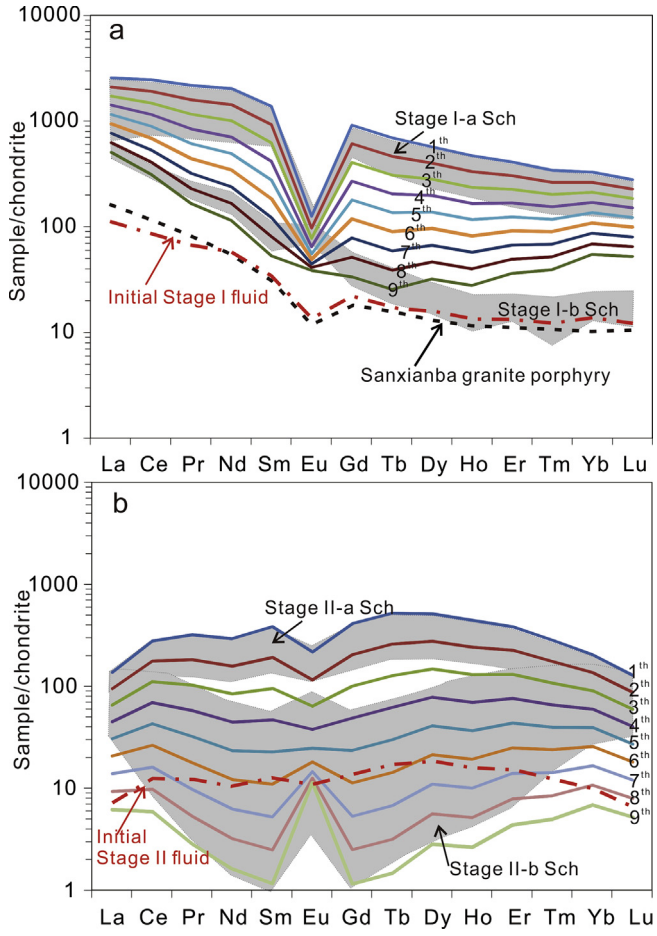

Fig. 11. Modelling of REE composition of scheelite during the batch fractionation of scheelite in Stage I (a) and Stage II (b). The shaded regions are REE patterns of scheelite samples and the solid lines represent the modeling REE patterns of different batches (marked as ordinal numeral) of scheelites. Chondritic values are from Sun and McDonough (1989). REE concentration of Sanxianba granite porphyry is from our unpublished data.

(Ballouard et al., 2016). As plagioclase was replaced by muscovite and sericite, Ca^{2+} was released into the fluids (Hemley and Jones, 1964). The elevated fluid Ca content promoted the precipitation of Stage I scheelite (e.g., Gibert et al., 1992; Liu et al., 2012; Seal et al., 1987; Wood and Samson, 2000). Stage I-a scheelite, inheriting the trace element composition of early magma-derived fluids, is LREE-enriched with negative Eu anomalies, and has high Mo, Mn, Nb, and Ta, but low Sr contents. Plagioclase decomposition released Eu and Sr, resulting in increased contents of these elements in the evolving fluid. Precipitation of hydrothermal minerals, such as scheelite and apatite, would have gradually lowered the REE, Nb, and Ta contents in the evolving fluids. These changes in fluid composition are recorded by Stage I-b scheelites.

In Stage II, the magmatic fluids were increasingly consumed, temperature decreased, and meteoric water infiltrated the fluid system (Pollard et al., 1991; Somarin and Ashley, 2004). Precipitation of Stage I scheelite (LREE-rich), apatite, molybdenite, and oxides significantly decreased the fluid REE (particularly LREE), Mo, Mn, Nb, and Ta contents. Recirculating meteoric waters that had interacted with Sr-rich basaltic rocks were incorporated into the mineralization system. These mixed fluids led to intense phyllic alteration (Reynolds and Beane, 1985; Taylor, 1974, 1997). The initial Stage II fluids were relatively depleted in LREE, Mo, Mn, Nb, and Ta, and they had flat REE patterns (Fig. 11b). Due to the addition of oxidizing and Sr-rich meteoric water, the Stage II fluids became relatively oxidized and Sr-rich. During phyllic alteration, plagioclase and K-feldspar were extensively replaced by sericite (Hemley and Jones, 1964). Feldspar decomposition led to the release of abundant Ca from plagioclase (Hemley and Jones, 1964) and P from alkali feldspar (Fryda and Breiter, 1995; London, 1992) into the fluids, and promoted the precipitation of Stage II scheelite and apatite. The fluids were consumed by extensive greisenization or lost from the system, resulting in the decreasing fluid/scheelite ratio during Stage II. Due to the low fluid/scheelite ratio, the trace element composition of scheelite was controlled mainly by the scheelite-fluid partition coefficients. Stage II-a scheelite preferentially incorporated the MREEs, given that the MREEs have the highest scheelite-fluid partition coefficients (Brugger et al., 2000; Zhao et al., 2018). Thus, precipitation of these MREE-rich scheelites would have gradually reduced the fluid MREE concentrations, leading to the progressive depletion of MREEs in Stage II-b scheelite (Fig. 7f).

The source of Ca is critical for scheelite mineralization. Unlike skarn scheelite deposits with carbonate wall rocks that provide Ca, most veinlet-disseminated scheelite mineralization in the Jiangnan Orogen is hosted by granitic rocks. This type of deposit cannot directly acquire sufficient Ca from the surrounding strata to produce mineralization. However, greisenization and phyllic alteration are extensive in such veinlet-disseminated W deposits (Jiang et al., 2015; Sun and Chen, 2017; Wang et al., 2017). As such, plagioclase decomposition during such alteration may provide the necessary Ca, and thus plays an important role in the W mineralization. We consider that this is the critical ore-forming mechanism responsible for the veinlet-disseminated W deposits in the Jiangnan Orogen.

7. Conclusions

1. Two stages of ore-forming fluids contributed to scheelite formation in the Muguayuan W deposit. Stage I fluids were relatively reduced, magma-derived, enriched in Mo, Mn, Nb, and Ta, and poor in Sr. Initial Stage I fluids were LREE-enriched and had negative Eu anomalies (Stage I-a), and evolved to Stage I-b fluids with positive Eu anomalies and low REE contents due to the precipitation of earlier hydrothermal minerals and greisenization.
2. Stage II ore-forming fluids resulted from the mixing of the evolved magmatic fluids with recirculating meteoric waters, and became relatively oxidized. These mixed fluids had low REE contents with a flat REE pattern. The precipitation of Stage II-a scheelite resulted in a marked reduction in fluid MREE contents and in the MREE-depletion of Stage II-b scheelite. Leaching of Sr from Ca-rich basaltic country rocks led to a significant increase in the Sr contents of Stage II fluids.
3. Plagioclase decomposition played a key role in the Muguayuan W mineralization, by providing the Ca in the fluids that allowed scheelite precipitation to take place.

Acknowledgements

This work is funded by the National Key R&D Program of China (2016YFC0600207), the National Natural Science Foundation of China (Grant No.41273053), the National Key Basic Research Program of China (Grant No.2012CB416702), the “CAS Hundred Talents” Project to Jian-Feng Gao (Grant No. Y5CJ03800). We sincerely thank Shi-Chang Luo and Hua Li from the No. 418 Geological Team of Bureau of Geology and Mineral Exploration and Development of Hunan Province, China for their help in field work. And we sincerely thank Liang Li from Nanjing FocuMS Technology Co. Ltd. for his technical assistance with LA-ICP-MS analyses.

Appendix A. Supplementary data

Supplementary data associated with this article can be found, in the online version, at https://doi.org/10.1016/j.oregeorev.2018.06.005.

References

Audetat, A., Gunther, D., Heinrich, C.A., 2000a. Causes for large-scale metal zonation around mineralized plutons: fluid inclusion LA-ICP-MS evidence from the Mole Granite, Australia. Econ. Geol. 95, 1563–1581.

Audetat, A., Gunther, D., Heinrich, C.A., 2000b. Magmatic-hydrothermal evolution in a fractionating granite: A microchemical study of the Sn-W-F-mineralized Mole Granite (Australia). Geochim. Cosmochim. Acta 64, 3373–3393.

Audetat, A., Pettke, T., 2003. The magmatic-hydrothermal evolution of two barren granites: A melt and fluid inclusion study of the Rito del Medio and Canada Pinabete plutons in northern New Mexico (USA). Geochim. Cosmochim. Acta 67, 97–121.

Bai, T.B., Groos, A.F.K., 1999. The distribution of Na, K, Rb, Sr, Al, Ge, Cu, W, Mo, La, and Ce between granitic melts and coexisting aqueous fluids. Geochim. Cosmochim. Acta 63, 1117–1131.

Ballouard, C., Poujol, M., Boulvais, P., Branquet, Y., Tartese, R., Vigneresse, J.L., 2016. Nb-Ta fractionation in peraluminous granites: A marker of the magmatic-hydrothermal transition. Geology 44, 231–234.

Beuchat, S., Moritz, R., Pettke, T., 2004. Fluid evolution in the W-Cu-Zn-Pb San Cristobal vein, Peru: Fluid inclusion and stable isotope evidence. Chem. Geol. 210, 201–224.

Bowman, J.R., Covert, J.J., Clark, A.H., Mathieson, G.A., 1985. The Cantung E Zone scheelite skarn orebody, tungsten, Northwest Territories: Oxygen, hydrogen, and carbon isotope studies. Econ. Geol. 80, 1872–1895.

Brugger, J., Lahaye, Y., Costa, S., Lambert, D., Bateman, R., 2000. Inhomogeneous distribution of REE in scheelites and the dynamics of Archaean hydrothermal systems (Mt. Charlotte and Drysdale gold deposits, Western Australia). Contrib. Mineral. Petrol. 139, 251–264.

Brugger, J., Etschmann, B., Pownceby, M., Liu, W., Grundler, P., Brewe, D., 2008. Oxidation state of europium in scheelite: Tracking fluid-rock interaction in gold deposits. Chem. Geol. 257, 26–33.

Chappell, B.W., White, A.J.R., 1992. I-type and S-type granites in the Lachlan Fold Belt. Trans. R. Soc. Edin. Earth Sci. 83, 1–26.

Chu, Y., Lin, W., Faure, M., Wang, Q.C., Ji, W.B., 2012. Phanerozoic tectonothermal events of the Xuefengshan Belt, central South China: Implications from U-Pb age and Lu-Hf determinations of granites. Lithos 150, 243–255.

Esmaeily, D., Nelelec, A., Valizadeh, M.V., Moore, F., Cotten, J., 2005. Petrology of the Jurassic Shah-Kuh granite (eastern Iran), with reference to tin mineralization. J. Asian Earth Sci. 25, 961–980.

Fryda, J., Breiter, K., 1995. Alkali feldspars as main phosphorus in rare-metal granites: Three examples from the Bohemian Massif (Czech Republic). Terr. Nova 7, 315–320.

Fu, J.Z., Xu, S.F., Wang, M.H., Hu, D.F., 2011. Geologic features and ore-controlling factors of Dongyuan tungsten and molybdenum deposit. Anhui Province Miner. Explor. 2, 501–511 (in Chinese with English Abstract).

Gao, Y.B., Li, W.Y., Li, Z.M., Wang, J., Hattori, K., Zhang, Z.W., Geng, J.Z., 2014. Geology, geochemistry, and genesis of tungsten-tin deposits in the Baiganhu district, northern Kunlun belt, Northwestern China. Econ. Geol. 109, 1787–1799.

Gaspar, L.M., Inverno, C.M.C., 2000. Mineralogy and metasomatic evolution of distal strata-bound scheelite skarns in the Riba de Alva Mine, Northeastern Portugal. Econ. Geol. 95, 1259–1275.

Ghaderi, M., Palin, J.M., Campbell, I.H., Sylvester, P.J., 1999. Rare earth element systematics in scheelite from hydrothermal gold deposits in the Kalgoorlie-Norseman region, Western Australia. Econ. Geol. 94, 423–438.

Gibert, F., Moine, B., Schott, J., Dandurand, J.L., 1992. Modeling of the transport and deposition of tungsten in the scheelite-bearing calc-silicate gneisses of the Montagne Noire, France. Contrib. Mineral. Petrol. 112, 371–384.

Green, T.H., 1995. Significance of Nb/Ta as an indicator of geochemical processes in the crust-mantle system. Chem. Geol. 120, 347–359.

Hazarika, P., Mishra, B., Pruseth, K.L., 2016. Scheelite, apatite, calcite and tourmaline compositions from the late Archean Hutti orogenic gold deposit: Implications for analogous two stage ore fluids. Ore Geol. Rev. 72, 989–1003.

He, A.S., Han, X.G., 1992. Characteristics and geological environment of volcanic rocks from Yiyang. Hunan Geol. 11, 269–274 (in Chinese with English Abstract).

Hemley, J.J., Jones, W.R., 1964. Chemical aspects of hydrothermal alteration with emphasis on hydrogen metasomatism. Econ. Geol. 59, 538–569.

Heinrich, C.A., 1990. The chemistry of hydrothermal tin (-tungsten) ore deposition. Econ. Geol. 85, 457–481.

HBGMR (Hunan Bureau of Geology and Mineral Resources), 1988. Regional Geology of the Hunan Province. Geological Press House, Beijing, p. 507 (in Chinese with English abstract).

Huang, L.C., Jiang, S.Y., 2014. Highly fractionated S-type granites from the giant Dahutang tungsten deposit in Jiangnan Orogen, Southeast China: Geochronology, petrogenesis and their relationship with W-mineralization. Lithos 202–203, 207–226.

Hu, R.Z., Fu, S.L., Huang, Y., Xiao, J.F., 2017. The giant South China Mesozoic low-temperature metallogenic domain: Reviews and a new geodynamic model. J. Asian Earth Sci. 137, 9–34.

Jiang, S.Y., Peng, N.J., Huang, L.C., Xu, Y.M., Zhan, G.L., Dan, X.H., 2015. Geological characteristic and ore genesis of the giant tungsten deposits from the Dahutang ore-concentrated district in northern Jiangxi Province. Acta Petrol. Sin. 31, 639–655.

Korges, M., Weis, P., Luders, V., Lüders, O., 2018. Depressurization and boiling of a single magmatic fluid as a mechanism for tin-tungsten deposit formation. Geology 46, 75–78.

Lecumberri-Sanchez, P., Vieira, R., Heinrich, C.A., Pinto, F., Walle, M., 2017. Fluid-rock interaction is decisive for the formation of tungsten deposits. Geology 45, 579–582.

Linnen, R.L., Samson, I.M., Williams-Jones, A.E., Chakhmouradian, A.R., 2014. Geochemistry of the rare earth element, Nb, Ta, Hf and Zr deposits. In: Turekian, H.D.H.K. (Ed.), Treatise on Geochemistry. Elsevier, Oxford, pp. 543–568.

Liu, Y., Deng, J., Li, C.F., Shi, G.H., Zheng, A.L., 2007. REE composition in scheelite and scheelite Sm-Nd dating for Xuebaoding W-Sn-Be deposit, Sichuan. Chin. Sci. Bull. 52, 2543–2550.

Liu, Y., Deng, J., Li, C.F., Shi, G.H., Sun, X., Yang, L.Q., 2012. Genesis of the Xuebaoding W-Sn-Be crystal deposits in Southwest China: Evidence from fluid inclusions, stable isotopes and ore elements. Resour. Geol. 62, 159–173.

Liu, Y.S., Hu, Z.C., Gao, S., Gunther, D., Xu, J., Gao, C.G., Chen, H.H., 2008. In-situ analysis of major and trace elements of anhydrous minerals by LA-ICP-MS without applying an internal standard. Chem. Geol. 257, 34–43.

Lu, H.Z., Liu, Y.M., Wang, C.L., Xu, Y.Z., Li, H.Q., 2003. Mineralization and fluid inclusion study of the Shizhuyuan W-Sn-Bi-Mo-F skarn deposit, Hunan province, China. Econ. Geol. 98, 955–974.

London, D., 1992. Phosphorus in S-type magmas: the P_2O_5 content of feldspars from peraluminous granites, pegmatites, and rhyolites. Am. Mineral. 77, 126–145.

Ma, D.S., Pan, J.Y., Lu, X.W., 2002. Geochemical signals for ore-forming process by mid-low temperature fluid in Au-Sb deposits in NW-Central Hunan, China. J. Nanjing University (Natural Sciences) 38, 453–1445.

Mangas, J., Arribas, A., 1988. Hydrothermal fluid evolution of the Sn-W mineralization in the Parrilla ore deposit (Caceres, Spain). J. Geol. Soc. 145, 147–155.

Manning, D.A.C., Henderson, P., 1984. The behavior of tungsten in granitic melt-vapor systems. Contrib. Mineral. Petrol. 86, 286–293.

Mao, J.W., Li, H.Y., 1996. Geology and metallogeny of the Shizhuyuan skarn-greisen W-Sn-Mo-Bi deposit, Hunan Province. Miner. Deposits 15, 1–15 (in Chinese with English abstract).

Mao, J.W., Xiong, B.K., Liu, J., Pirajno, F., Cheng, Y.B., Ye, H.S., Song, S.W., Dan, P., 2017. Molybdenite Re-Os dating, zircon U-Pb age and geochemistry of granitoids in the Yangchuling porphyry W-Mo deposit (Jiangnan tungsten ore belt), China: Implications for petrogenesis, mineralization and geodynamic setting. Lithos 286–287, 35–52.

Mao, Z.H., Cheng, Y.B., Liu, J.J., Yuan, S.D., Wu, S.H., Xiang, X.K., Luo, X.H., 2013. Geology and molybdenite Re-Os age of the Dahutang granite-relatedveinlet-disseminated tungsten ore field in the Jiangxi Province, China. Ore Geol. Rev. 53, 422–433.

Mao, Z.H., Liu, J.J., Mao, J.W., Deng, J., Zhang, F., Meng, X.Y., Xiong, B.K., Xiang, X.K., Luo, X.H., 2015. Geochronology and geochemistry of granitoids related to the giant Dahutang tungsten deposit, middle Yangtze River region, China: Implications for petrogenesis, geodynamic setting, and mineralization. Gondwana Res. 28, 816–836.

Marshall, D.J., 1988. Cathodoluminescence of Geological Materials. Unwin Hyman, Boston & London.

Miles, A.J., Graham, C.M., Hawkesworth, C.J., Gillespie, M.R., Hinton, R.W., Bromiley, G.D., 2014. Apatite: A new redox proxy for silicic magmas? Geochim. Cosmochim. Acta 132, 101–119.

Peng, J.T., Hu, R.Z., Zhao, J.H., Fu, Y.Z., Yuan, S.D., 2004. Rare earth element (REE) geochemistry for scheelite from the Woxi Au-Sb-W deposit, western Hunan. Geochimical 34, 115–122 (in Chinese with English abstract).

Peng, J.T., Hu, R.Z., Zhao, J.H., Fu, Y.Z., Yuan, S.D., 2003. The ore-forming fluid with a marked radiogenic ^{87}Sr signature from the Woxi Au-Sb-W deposit and its significant implications. Bull. Mineral. Petrol. Geochem. 22, 193–196 (in Chinese with English abstract).

Pirajno, F., 2009. Intrusion-related hydrothermal mineral systems. In: Hydrothermal Processes and Mineral Systems. Springer, London, pp. 205–259.

Pollard, P.J., Andrew, A.S., Taylor, R.G., 1991. Fluid inclusion and stable isotope evidence for interaction between granites and magmatic hydrothermal fluids during formation of disseminated and pipe-style mineralisation at the Zaaiplaats tin mine. Econ. Geol. 86, 121–141.

Pollard, P.J., 1983. Magmatic and postmagmatic process in the formation of rocks associated with rare-element deposits. Inst. Mining Metallurgy Trans. 92, 1–9.

Prowatke, S., Klemme, S., 2006. Trace element partitioning between apatite and silicate melts. Geochim. Cosmochim. Acta 70, 4513–4527.

Raimbault, L., Baumer, A., Dubru, M., Benkerrou, C., Croze, V., Zahm, A., 1993. REE fractionation between scheelite and apatite in hydrothermal conditions. Am. Mineral. 78, 1275–1285.

Reynolds, T.J., Beane, R.E., 1985. Evolution of hydrothermal characteristics at the Santa Rita, New Mexico, porphyry copper deposit. Econ. Geol. 80, 1328–1347.

Schwartz, M.O., Surjono, 1990. Greisenization and albitization at the Tikus tin-tungsten deposit, Belitung, Indonesia. Econ. Geol. 85, 691–713.

Seal, R.R.I.I., Clark, A.H., Morrissey, C.J., 1987. Stockwork tungsten (scheelite)- molybdenum mineralization, Lake George, southwestern New Brunswick. Econ. Geol. 82, 1259–1282.

Seedorff, E., Dilles, J.H., Proffett Jr., J.M., Einaudi, M.T., Zurcher, L., Stavast, W.J.A., Johnson, D.A., Barton, M.D., 2005. Porphyry deposits: Characteristics and origin of hypogene features. Econ. Geol. 100th Annv., 251–298.

Shapovalov, Y.B., Setkova, T.V., 2012. Experimental study of mineral equilibria in the system K_2O (Li_2O)-Al_2O_3-SiO_2-H_2O-HF at 300 to 600 °C and 100 MPa with application to natural greisen systems. Am. Mineral. 97, 1452–1459.

Sinclair, W.D., Gonevchuk, G.A., Korostelev, P.G., Semenyak, B.I., Rodionov, S., Seltmann, R., Štemprok, M., 2011. World distribution of tin and tungsten deposits. Geological Survey of Canada, Open File 5482, scale 1: 35,000,000.

Smith, M.P., Henderson, P., Jeffries, T.E.R., Long, J., Williams, C.T., 2004. The rare earth elements and uranium in garnets from the Beinn an Dubhaich Aureole, Skye, Scotland, UK: Constraints on processes in a dynamic hydrothermal system. J. Petrol. 45, 457–484.

Somarin, A.K., Ashley, P., 2004. Hydrothermal alteration and mineralisation of the Glen Eden Mo-W-Sn deposit: A leucogranite-related hydrothermal system, Southern New England Orogen, NSW, Australia. Miner. Deposits 39, 282–300.

Song, G.X., Qin, K.Z., Li, G.M., Evans, N.J., Chen, L., 2014. Scheelite elemental and

isotopic signatures: Implications for the genesis of skarn-type W-Mo deposits in the Chizhou area, Anhui Province, Eastern China. Am. Mineral. 99, 303–317.
Štemprok, M., Seltmann, R., 1994. The metallogeny of the Erzgebirge (Krušné hory). In: Seltmann, K., Mier (Eds.), Metallogeny of Collisional Orogens. Czech Geological Survey, pp. 61–69.
Štemprok, M., 1987. Grensenization (a review). Geol. Rundschau 76, 169–175.
Štemprok, M., Pivec, E., Langrová, A., 2005. The petrogenesis of a wolframite-bearing greisen in the Vykmanov granite stock, Western Krušné hory pluton (Czech Republic). Bull. Geosci. 80, 163–184.
Sun, K.K., Chen, B., 2017. Trace elements and Sr-Nd isotopes of scheelite: Implications for the W-Cu-Mo polymetallic mineralization of the Shimensi deposit, South China. Am. Mineral. 102, 1114–1128.
Sun, S.S., McDonough, F., 1989. Chemical and isotopic systematics of ocean basalts: Implications for mantle composition and processes, in Magmatism in the Ocean Basins. In: Saunders, A.D., Norry, M.J. (Eds.), Magmatism in the Ocean Basins. Geological Society of London Special Publication, pp. 313–345.
Taylor, H.P., 1974. The application of oxygen and hydrothermal isotope studies to problems of hydrothermal alteration and ore deposition. Econ. Geol. 69, 843–883.
Taylor, H.P., 1997. Oxygen and hydrogen isotope relationships in hydrothermal mineral deposits. In: Barnes, H.L. (Ed.), Geochemistry of Hydrothermal Ore Deposits, third ed. John Wiley, New York, pp. 229–302.
Xiang, X.K., Wang, P., Zhan, G.N., Sun, D.M., Zhong, B., Qian, Z.Y., Tang, R., 2013. Geological characteristics of Shimensi tungsten polymetallic deposit in northern Jiangxi Province. Miner. Deposits 32, 1171–1187 (in Chinese with English Abstract).
Xiao, X.D., 1983. On the basaltic komatiite and its formative environment in Yiyang, Hunan. J. Central-South Inst. Min. Metall. 38, 106–113 (in Chinese with English Abstract).
Xie, G.Q., Mao, J.W., Li, W., Fu, B., Zhang, Z.Y., 2018. Granite-related Yangjiashan tungsten deposit, southern China. Miner. Deposits. http://dx.doi.org/10.1007/s00126-018-0805-5.
Xiong, Y.Q., Shao, Y.J., Zhou, H.D., Wu, Q.H., Liu, J.P., Wei, H.T., Zhao, R.C., Cao, J.Y., 2017. Ore-forming mechanism of quartz-vein-type W-Sn deposits of the Xitian district in SE China: Implications from the trace element analysis of wolframite and investigation of fluid inclusions. Ore Geol. Rev. 83, 152–173.
Wang, H., Feng, C.Y., Li, D.X., Xiang, X.K., Zhou, J.H., 2015. Sources of granitoids and ore-forming materials of Dahutang tungsten deposit in northern Jiangxi Province: Constrains from mineralogy and isotopic tracing. Acta Petrol. Sin. 31, 725–739.
Wang, K.X., Chen, P.R., Chen, W.F., Ling, H.F., Zhao, K.D., Yu, Z.Q., 2012. Magma mingling and chemical diffusion in the Taojiang granitoids in the Hunan Province, China: Evidences from petrography, geochronology and geochemistry. Miner. Petrol. 106, 243–264.
Wang, X.C., Li, X.H., Li, W.X., Li, Z.X., 2007a. Ca. 825 Ma komatiitic basalts in South China: First evidence for > 1500 °C mantle melts by a Rodinian mantle plume. Geology 35, 1103–1106.
Wang, X.L., Zhou, J.C., Qiu, J.S., Gao, J.F., 2004. Geochemistry of the Meso- to Neoproterozoic basic-acid rocks from Hunan Province, South China: Implications for the evolution of the western Jiangnan orogeny. Precambrian Res. 133, 17–103.
Wang, X.L., Zhou, J.C., Griffin, W.L., Wang, R.C., Qiu, J.S., O'Reily, S.Y., Xu, X.S., Liu, X.M., Zhang, G.L., 2007b. Detrital zircon geochronology of Precambrian basement sequences in the Jiangnan Orogen: Dating the assembly of the Yangtze and Cathaysia Blocks. Precambrian Res. 159, 117–131.
Wang, X.L., Zhou, J.C., Griffin, W.L., Zhao, G.C., Yu, J.H., Qiu, J.S., Zhang, Y.J., Xing, G.F., 2014. Geochemical zonation across a Neoproterozoic orogenic belt: Isotopic evidence from granitoids and metasedimentary rocks of the Jiangnan Orogen, China. Precambrian Res. 242, 154–171.
Wang, Y.Y., Kerkhof, A.V.D., Xiao, Y.L., Sun, H., Yang, X.Y., Lai, J.Q., Wang, Y.G., 2017. Geochemistry and fluid inclusions of scheelite-mineralized granodiorite porphyries from southern Anhui Province, China. Ore Geol. Rev. 89, 988–1005.
Webster, J., Thomas, R., Förster, H.J., Seltmann, R., Tappen, C., 2004. Geochemical evolution of halogen-enriched granite magmas and mineralizing fluids of the Zinnwald tin-tungsten mining district, Erzgebirge, Germany. Miner. Deposits 39, 452–472.
Werner, A.B.T., Sinclair, W.D., Amey, E.B., 2014. International strategic mineral issues summary report—Tungsten (ver. 1.1, November 2014): U.S. Geological Survey Circular 930–O, p. 74, http://pubs.usgs.gov/circ/0930/o/. [Supersedes version 1.0 published in 1998; revisions in 2014 by John H. DeYoung, Jr., and Kim B. Shedd.].
White, D.E., 1955. In: Thermal Springs and Epithermal Ore Deposits. Econ. Geol., pp. 99–154.
Wood, S.A., Samson, I.M., 2000. The hydrothermal geochemistry of tungsten in granitoid environments: I. Relative solubilities of ferberite and scheelite as a function of T, P, pH, and *mNaCl*. Econ. Geol. 95, 143–182.
Wu, S.H., Wang, X.D., Xiong, B.K., 2014. Fluid inclusion studies of the Xianglushan skarn tungsten deposit, Jiangxi Province, China. Acta Petrol. Sin. 30, 178–188.
Zajacz, Z., Halter, W.E., Pettke, T., Guillong, M., 2008. Determination of fluid/melt partition coefficients by LA-ICPMS analysis of co-existing fluid and silicate melt inclusions: Controls on element partitioning. Geochim. Cosmochim. Acta 72, 2169–2197.
Zhao, W.W., Zhou, M.F., Williams-Jones, A.E., Zhao, Z., 2018. Constraints on the uptake of REE by scheelite in the Baoshan tungsten skarn deposit, South China. Chem. Geol. 477, 123–136.
Zhou, M.F., Yan, D.P., Kennedy, A.K., Li, Y., Ding, J., 2002. SHRIMP U-Pb zircon geochronological and geochemical evidence for Neoproterozoic arc-magmatism along the western margin of the Yangtze Block, South China. Earth Planet Sci. Lett. 196, 51–67.
Zhou, X.M., Zhu, Y.H., 1993. Petrological evidences of Neoproterozoic collision-orogenic and suture belts in southeastern China. In: Li, J.L. (Ed.), Lithospheric Structures and Geological Evolution in Continent from Southeastern China. Metallurgical Industry Press, Beijing, pp. 87–97 (in Chinese).